

Marshall University

Marshall Digital Scholar

Theses, Dissertations and Capstones

2018

Design and simulation of a pneumatic actuator bending soft robotics based on 3D printing

Chenyu Zheng

Follow this and additional works at: <https://mds.marshall.edu/etd>



Part of the [Robotics Commons](#)

**DESIGN AND SIMULATION OF A PNEUMATIC ACTUATOR BENDING SOFT
ROBOTICS BASED ON 3D PRINTING**

A thesis submitted to
the Graduate College of
Marshall University
In partial fulfillment of
the requirements for the degree of
Master of Science

In
Mechanical Engineering
by

Chenyu Zheng

Approved by

Dr. Ana Pena Alvarez, Committee Chairperson

Dr. Iyad Hijazi

Dr. Roozbeh Ross Salary

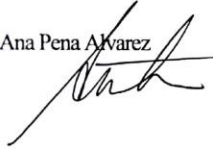
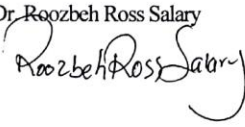
Marshall University
December 2018

ACKNOWLEDGMENTS

I appreciate the mentorship provided by Dr. Ana Pena Alvarez. Without her guidance, this work would not have been possible. This last year has been beyond stressful for the both of us, for a variety of reasons, and I appreciate the kick to make sure I got everything done, and not giving up until the thesis is done. I would like to thank my committee members Dr. Iyad Hijazi and Roozbeh Ross Salary who gave me so many suggestions to improve the quality of the thesis. I'm also grateful for the laboratory assistant provided by James Kuzma and Daniel Egnatoff.

APPROVAL OF THESIS

We, the faculty supervising the work of Chenyu Zheng, affirm that the thesis, *Design and Simulation of a Pneumatic Actuator Bending Soft Robotics Based On 3D Printing*, meets the high academic standards for original scholarship and creative work established by the College of Information Technology and Engineering for the Master of Science in Mechanical Engineering. This work also conforms to the editorial standards of our discipline and the Graduate College of Marshall University. With our signatures, we approve the manuscript for publication.

Dr. Ana Pena Alvarez 	Committee Chairperson	Date 12/14/2018
Dr. Iyad Hijazi 	Committee Member	Date 12/14/2018
Dr. Roozbeh Ross Salary 	Committee Member	Date 12/14/2018

© 2018
Chenyu Zheng
ALL RIGHTS RESERVED

TABLE OF CONTENTS

LIST OF TABLES	viii
LIST OF FIGURES	ix
ABSTRACT	ix
CHAPTER 1 INTRODUCTION	1
1.1. Background of soft robotics.....	4
1.1.1. McKibben Muscle.....	4
1.1.2. Pleated Pneumactical Artificial Muscle (Pleated PAM)	6
1.1.3. Sleeved braid muscle	7
1.1.4. Yariott Muscle	8
1.1.5. ROMAC.....	8
1.1.6. Pneu-Net	9
1.2. Background of 3D printing	10
1.2.1. Selective Laser Sintering/Melting.....	11
1.2.2. Fused Deposition Modeling.....	12
1.2.3. Stereo Lithography Apparatus	12
1.2.4. Direct Metal Laser Sintering.....	13
1.3. Background of topology	13
1.4. Kinematic Analysis.....	15
CHAPTER 2 THEORETICAL BACKGROUND.....	16
CHAPTER 3 DESIGN AND MODELING.....	27
3.1. Design	27

3.2. Traditional casting fabrication	28
CHAPTER 4 SIMULATION	31
4.1. Creating geometry model.....	31
4.2. Simulation in ANSYS with linear properties of material	31
4.3. Simulation in ANSYS with nonlinear properties of material	36
Neo-Hookean model	36
Mooney-Rivlin model.....	36
Yeoh model.....	37
CHAPTER 5 3D PRINTING PRODUCT EXPERIMENT	41
5.1. Optimization of 3D printing setting	45
CHAPTER 6 EXPERIMENT	49
CHAPTER 7 CONCLUSION.....	55
REFERENCES	57
APPENDIX A.....	65
The Office of Research Integrity Approval Letter.....	66
APPENDIX B	69
Data From Simulations and Experiment.....	66
APPENDIX C	69
Matlab code.....	69
Displacement_linear_simulation_vs_theoretical.m	69

Displacement_nonlinear_simulation_vs_theoretical.m	70
Displacement_exp.m.....	71
Displacement_linear_nonlinear.m	73
hyperelastic_curve.m	75
Curve1.m.....	76
Curve2.m.....	78
APPENDIX D.....	80
G-code for 3d printing	80
Start Gcode.....	80
End Gcode.....	81

LIST OF TABLES

1.	Characteristics of different types of hard and soft robots.....	4
2.	The properties of NinjaFlex.....	32
3.	Yeoh hyperelastic parameters in ANSYS.....	38
4.	The design length and actual length for each direction of printed model.....	44
5.	Data collected from linear material simulation in ANSYS.....	66
6.	Data collected from nonlinear material simulation in ANSYS.....	66
7.	Data collected from experiments.....	67
8.	Data collected from different thickness of side walls in ANSYS.....	68
9.	Data collected from different thickness of the wall over the channel in ANSYS...	68

LIST OF FIGURES

1. Rigid robotic hand.....	2
2. Hyper-redundant robot manipulator	3
3. Hard continuum actuator.....	3
4. McKibben muscle	6
5. Pleated pneumatic artificial muscle shape	7
6. The shape of romac	9
7. Pneu-Net gripper experiment.....	10
8. The Pneu-Net chamber before (a) and after (b) inflated.....	16
9. The range of motion of a single pneumatic actuator.....	19
10. The schematic diagram of a cantilever beam with uniform distributed load.....	20
11. 3d sketch for pneunets actuator by creo 4.0.....	28
12. Processing overview for traditional pneumatic bending actuators fabrication	29
13. Three views and isometric view of Pneu-Net actuator (units: mm)	31
14. Schematic diagram of meshing in ansys.....	33
15. The place of monitor edge	34
16. The linear material properties simulation results under different pressures	35
17. The pressure-deformation curve comparison chart of linear material properties simulation results under different pressures in x-direction.....	35

18. The pressure-deformation curve comparison chart of linear material properties simulation results under different pressures in y-direction.....	36
19. Stress–strain curves for various hyperelastic material models	37
20. The pressure-deformation comparison chart of nonlinear material properties simulation results under different pressures in x-direction.....	38
21. The pressure-deformation comparison chart of nonlinear material properties simulation results under different pressures in y-direction.....	39
22. The nonlinear material properties simulation results under different pressures	39
23. Comparison between linear, nonlinear material properties simulation and theoretical in x-direction.....	40
24. Comparison between linear, nonlinear material properties simulation and theoretical in y-direction.....	40
25. Folger Tech Ft-5 R2 large scale 3d printer	41
26. Finished product after dragging phenomenon	43
27. Finished product after scorch phenomenon	43
28. The coordinate system of printing area.....	45
29. The printed “flow” samples (from left to right:100%, 105%, 110%, 115%, 120%)..	46
30. Microscopy images for different flow settings at the samples’ edges	47
31. Microscopy images for different flow settings at the samples’ center	48

32. The schematic diagram of experiment equipment	50
33. The process of bending for Pneu-Net actuator	51
34. Comparison between experiment results, simulation, and theoretical in x-direction .	51
35. Comparison between experiment results, simulation, and theoretical in y-direction .	52
36. Comparison between different thickness of side walls.....	53
37. Comparison between different thickness of walls over channel.....	54
38. The touch situation at the same thickness of side walls in different pressure	54

ABSTRACT

Robots mechatronic devices are able to replicate human actions, especially in dangerous environments and in manufacturing. Recently, the development of robotics has been inspired by bionics. The advanced robotics allow advanced robots to be used in new environments where they were not traditionally applicable, such as narrow and small spaces. Compared to traditional rigid robots, soft robots are made by deformable materials and possess high dexterity and adaptivity in harsh working environments.

Traditional soft robots are made by casting. The method implies that the molds of soft robots should be designed and printed by a 3D printer first, before casting. In this thesis, a pneumatic bending actuator will be designed and printed by 3D printer directly. The direct 3D printing method saves abundant time in the overall design and printing as in rubber casting. The printing material is a hyperelastic material called NinjaFlex.

Moreover, this thesis simplified the physical model to a cantilever beam with uniform distributed load. Based on the cantilever mathematical model, two types of simulation have been designed with linear material properties and nonlinear material properties. The wall thickness of the original design was set as the optimization parameters. By adjusting the thickness, the relationship between the wall thickness and the deformation of the bending actuator was obtained. By comparing the results of experiments, simulation, and theoretical modeling, we propose 3D printing of soft actuators as a novel technique to be used in the new frontier of soft robotics.

CHAPTER 1

INTRODUCTION

Robotics is a cross-subject which includes the design, production, manipulation and application of robots. Mechanical engineering, computer science, and electronic engineering mutually combine to design these automatic machines, which are able to replace humans for repetitive work or high precision operation, especially in dangerous environments. Recently, the development of robotics has been inspired by bionics, which allows advanced robots to be applied in many new environments where they were not traditionally applicable, such as narrow and small spaces [1].

Based on the compliance of the underlying materials, robots can be classified as rigid robots or soft robots. The traditional rigid robots have been developed for decades. However, they are limited by their rigid structure, which cannot always be adapted to all working environments. Their rigid frames and connections are applied in almost every traditional rigid robotic system. The rigid robotics usually face trouble while working in narrow and highly crowded environments. Also, if the working space is exceptionally complicated, the working motion routes cannot be programmed.

In contrast, many animals and plants display their soft structure in complicated movements, such as the trunks of elephants and the tentacles of the octopus. Those soft muscle structures are typical muscular hydrostats which can be used as an inspiration to design soft robots [2].

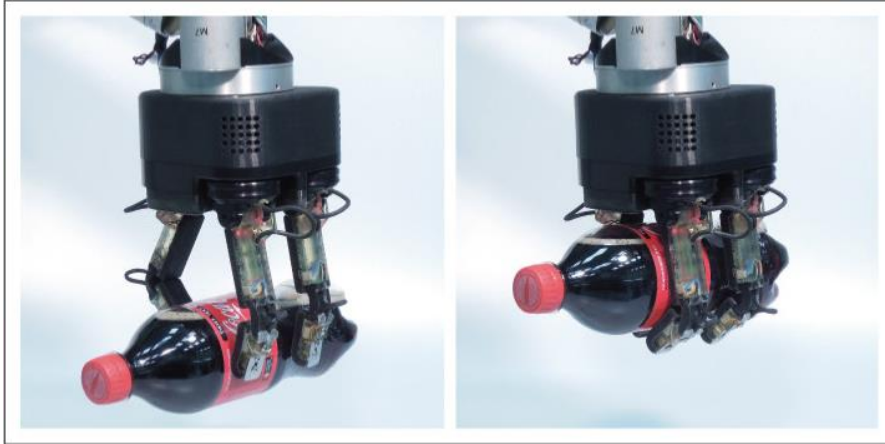


Figure 1 Rigid robotic hand [3]

In 1948, Norbert Wiener introduced cybernetics, a transdisciplinary science, which rapidly became the base of robotics [4]. With the growth of this field, robots have developed into four types, depending on the type of actuators: rigid (Figure 1), hyper-redundant (Figure 2), hard continuum (Figure 3), and soft robots. The detailed characteristics of those four types are shown in Table 1 Characteristics of different types of hard and soft robots [2]. Rigid robots are the most common type. Since these robots can operate with repeated motion and accurately by a programming action route, they are used in well-defined environments. In rigid-body robotics, the number of degrees of freedom (DOF) equals their total amount of rotation and translation motions. When rigid robots have abundant DOFs, they become hyper-redundant robots. Hard continuum robots are also a type of hard robots since most of them are made in shape memory alloys. Although their material is stiff in a normal operation, they present, or they exhibit a continuum as they have infinite DOF.

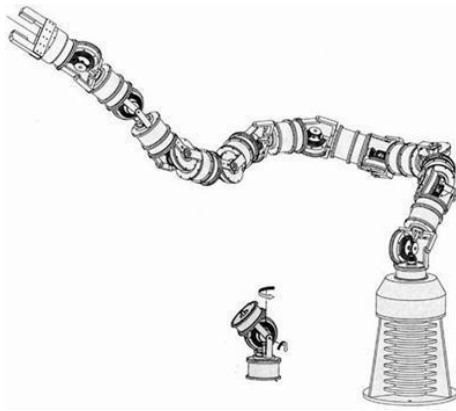


Figure 2 Hyper-redundant robot manipulator [5]



Figure 3 Hard continuum actuator [6]

Compared to traditional hard robots, soft robots are made by extensive deformable materials such as rubber and other polymers. Those “soft” materials can absorb energy from collision and compression. Just as hard-continuum robots, the structures of soft robots are also continuous and have infinite degrees of freedom. For this reason, soft robots have high dexterity and exhibit adaptivity in working environments [5].

Table 1 Characteristics of different types of hard and soft robots [2]

	Rigid	Hyper-redundant	Hard continuum	Soft
Properties				
Degrees of freedom	Few	Large	Infinite	Infinite
Actuators	Few, discrete	Many, discrete	Continuous	Continuous
Materials stain	None	None	Small	Large
Materials	Metals, plastics	Metals, plastics	Shape memory alloy	Rubber, electroactive polymer
Capabilities				
Accuracy	Very high	High	High	Low
Load capacity	High	Lower	Lower	Lowest
Safety	Dangerous	Dangerous	Dangerous	Safe
Dexterity	Low	High	High	High
Working environment	Structured only	Structured and unstructured	Structured and unstructured	Structured and unstructured
Manipulable objects	Fixed sized	Variable size	Variable size	Variable size
Conformability to obstacles	None	Good	Fair	Highest
Design				
Controllability	Easy	Medium	Difficult	Difficult
Path planning	Easy	Harder	Difficult	Difficult
Position sensing	Easy	Harder	Difficult	Difficult
Inspiration	Mammalian limbs	Snakes, fish	Trunks, tentacles	Muscular hydrostats

1.1. Background of soft robotics

1.1.1. McKibben Muscle

McKibben Muscle is a type of soft robotic actuator which consists of a cylindrical braided muscle and was introduced by Joseph L. McKibben in the late 1950s to assist paralyzed patients [6-8]. It is a type of pneumatical artificial muscle which is frequently used as a research object, and is well-developed and suggested as a primitive soft robotic actuator similar to animal muscle [9]. The basic structure of the McKibben Muscle contains two main parts as shown in

Figure 4: the inner tube and the braided sleeving. The inner layer is made from rubber or latex, with two metal plugs which have been sealed in both ends of the tube. The braided sleeving, which is typically inextensible, is usually made from Nylon fiber, and it is also fixed at both ends of the tube [10-12]. By changing the weave angle θ , the braid diameter and length can also be changed. The maximum volume of the braid is attained when the weave angle is equal to 54.7° to 59.3° , and it follows the equation [13-15]:

$$V = \frac{l_s^3}{4\pi N^2} \cos\theta \sin^2\theta \quad (1)$$

Where l_s is the length of each braid strand, and N is an amount of encirclements around the tube. The value of the weave angle cannot be greater than the angle in maximum volume unless the artificial muscle is compressed in the longitudinal axis. The tensile force can be related to the weave angle though the equation also has relation with weave angle [6, 14, 16-18], as equation (65) shows,

$$F = \frac{\pi D_{max}^2 p}{4} (3\cos^2\theta - 1) \quad (2)$$

Where p is the control pressure; D_{max} is the diameter of the braid at weave angle equal to 90° .

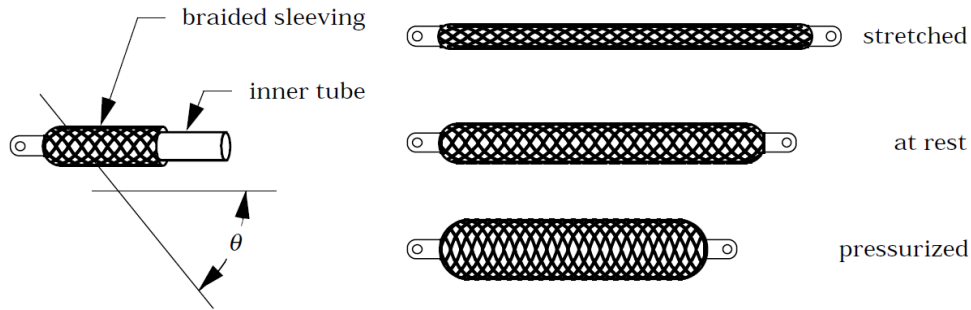


Figure 4 McKibben muscle

1.1.2. Pleated Pneumactical Artificial Muscle (Pleated PAM)

To eliminate hysteresis and material deformation, a re-arranged muscle was developed by Daerden in 1999 [13, 19, 20]. Pleated PAM consists of a membrane which has many pleats in the axial direction. When unpressurized, it is shaped like a car filter. However, when this muscle is stressed, it shortens and begins to swell, like a pumpkin, as shown in Figure 5 [14]. Its membrane has a high tensile stiffness to eliminate rubber-like strain, but it also has a high degree of flexibility, such as the Kevlar fabric [19]. Because the flap is arranged radially, the process of folding and deployment does not involve friction, and hysteresis does not occur when associated with friction. In addition, since it does not need significant energy to expand, there is no loss of output power.

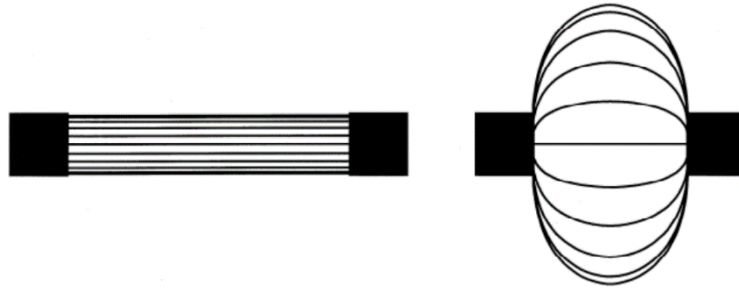


Figure 5 Pleated Pneumatical Artificial Muscle shape

Another purpose of such a pleated arrangement is that there is no parallel stress so that maximum expansion and thus contraction can be expected. An ideal way to achieve this is to use an orthotropic film having a high tensile stiffness in one direction and a modulus of elasticity that can be zero perpendicular to that direction. The pleated membrane is the way to approximate this pattern of expansion: the more folds, the shallower they become, hence, a better approximation.

1.1.3. Sleeved braid muscle

To produce a simple, lightweight, powerful, and inexpensive pneumatic braid actuator, Winters proposed a sleeved bladder muscle prototype in 1989 [21, 22]. The shape of this artificial muscle looks like the McKibben muscle, and it consists of a bladder in a braid directly connected to a cord which can provide tensile strength. According to Winters' experiment, this design could reduce outside braid price to under \$1 for two cords per actuator. However, the cost of this inexpensive approach is that the weave angle is pre-set to 20-30 degrees, which means the motion range of sleeved braid muscle is smaller than other types of artificial muscles [23].

1.1.4. Yariott Muscle

Yariott patented this type of fluid muscle in 1972 [24]. The shape of the Yariott muscle is a football-like bladder which is spirally coiled by a series of cords from one end to another. Also, there are several tendons in the axial line. Those cords focus on resisting bladder expansion when pressured. Only a helical cord wind around the bladder is also available [14]. In principle, Yariott muscle and Sleeved braid muscle are more suitable for low pressure movement instead of highly pressurized.

1.1.5. ROMAC

ROMAC (robotic muscle actuator) was patented by Guy Immega and Mirko Kukolj in 1990 [25]. According to the invention, this is an axially contractible actuator. The actuator includes a hollow shell, which is a membrane that is undeformable and permeable. The membrane has the appearance of a polyhedron, and each surface includes at least three edges (Figure 6). Due to the tensile stiffness of the membrane, this design allows the actuator to change the volume and to keep the total surface almost constant. The length of the actuator is usually between 6 cm and 30 cm, but there is a miniature version of 1-6 cm. For regular sizes, 50% shrinkage was reported under pressure up to 700kPa, while 4500N and 13600N [14, 26].

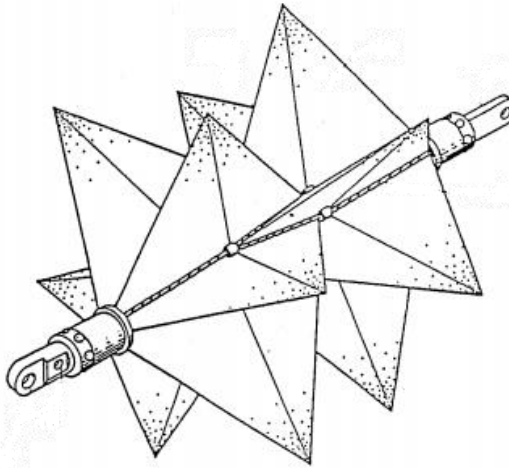


Figure 6 The shape of ROMAC[25]

1.1.6. Pneu-Net

The pneumatical McKibben type actuator is a highly developed soft actuator, but it is more like a single muscle fiber in motion, whether it be in contraction or stretching. Furthermore, the pneumatically driven flexible microactuators (FMAs) have been proven to be able to perform accurate bending, grabbing, and even manipulating objects [27, 28]. Ilievski et al. [29] introduced a new pneumatically driven actuator called the Pneu-Net. Based on the solid elastomer of the original cuboid, several hollow, parallel, equal-volume chambers are embedded in a single, continuous structure. In their experiments (Figure 7), a tip-to-tip 14 cm starfish-like gripper can grab and hold a 10 cm diameter, 300 grams spherical object. Moreover, in the live capture experiment, the gripper successfully grabbed an anesthetized mouse and did not hurt it. During the experiment, the actuator was able to keep its shape with no significant changes for 10 minutes without continuously filling the actuator with air.

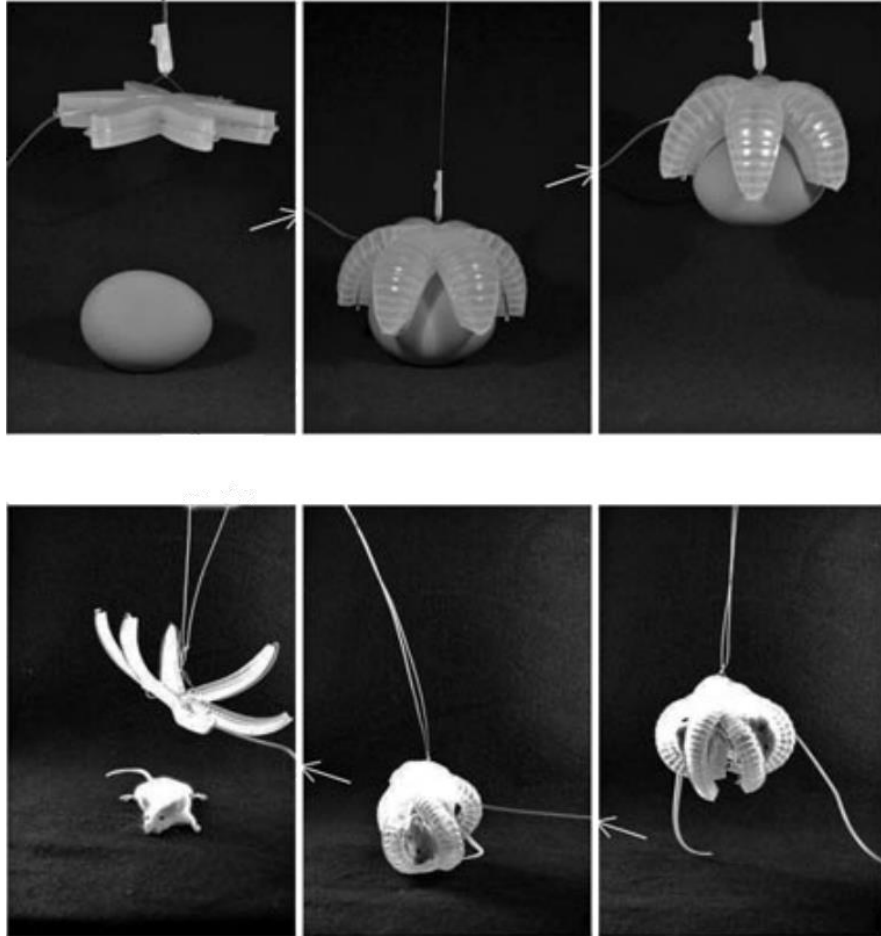


Figure 7 Pneu-Net gripper experiment[29]

1.2. Background of 3D printing

Early additive manufacturing (AM) equipment and materials were developed in the 1980s. In 1981, Xiao Yuxiu, from the Industrial Research Institute of Nagoya City, invented two methods for manufacturing three-dimensional plastic models using additive materials of polymers, whose ultraviolet irradiation area was controlled by a mask pattern or a scanning fibre optic transmitter [30, 31]. Then, in 1984, Chuck Hull of 3D Systems Inc. invented stereolithography, curing polymer photopolymers with UV lasers, and laminating raw materials [32]. The term “3D printing” first used the process of using standard conventional inkjet printer

nozzles. Until now, most 3D printers, especially those used by 3D printing enthusiasts and consumer-designed 3D printers, use mostly the fused deposition modeling method.

With the digital data from any 3D model or another electronic data source, the objects can be created in any shape or geometry. The real shape of 3D objects can be transferred into digital data and 3D digital models by 3D scanning. Before printing a 3D model, one of the most important steps is called “repair” to examine errors, since most computer-aided design (CAD) applications may produce errors such as holes, self-intersections, and manifold errors [33]. After finishing repairing, models in STL files can be converted into a series of thin layers by a software called a “slicer,” which can also produce a G-code that gives the instruction to a 3D printer [34]. By following the G-code commands, the 3D printer combines layers of liquid, powder, paper, or sheet material to form different cross-sections. After that, the assembled body of those printed layers is the final 3D printing product.

By using 3D technology, it is possible to print anything such as clothes, jewelry, drugs, and even guns [35]. With the wide range of applications, the implementation of 3D printing is increasing rapidly. In 2014, the 3D printing industry was worth \$700 million, and the number is expected to increase to \$8.9 billion by 2024 [36]. According to the different technologies of 3D printing, several types of 3D printers are usually used: Selective Laser Sintering/Melting (SLS/SLM), Fused Deposition Modeling (FDM), Stereo Lithography Apparatus (SLAs), and Direct Metal Laser Sintering (DMLS).

1.2.1. Selective Laser Sintering/Melting

Selective Laser Sintering/Melting (SLS/SLM) printers use a laser to select a suitable powdered material such as powdered wax, ceramic, metal, or nylon to print new objects [37, 38]. The SLS/SLM is a technique in which a roller spreads powder on the sintering platform forming

a thin layer of 100 mm diameter alumina cylinder [39]. The term SLS or SLM is chosen depending on the composition of the powder and the density of laser energy [40, 41]. The main drawback of this technique is the high pore volume fraction of the final 3D objects since porosity decreases due to the temperature of a post-sintering process under air or vacuum [42]. In addition, some materials used for this technique such as aluminum powder inherently form a tenacious surface oxide film. However, SLS/SLM is still chosen by manufacturers due to its high quality, and reliable materials, such as aluminum alloy powder [43].

1.2.2. Fused Deposition Modeling

Another common method of 3D printing which uses polymer filaments is Fused Deposition Modeling [44]. Compared to SLS printers, FDM printers are more common and cheaper [37]. Instead of using powder, FDM printers produce a highly accurate object by heating a continuous filament of a thermoplastic polymer from a temperature-controlled print head. After reaching a semi-liquid state, the filament is extruded on the platform of printed layers [44]. If an FDM printer is improved in its complexity and cost, its capabilities may be extended to multiple printheads [37]. The main advantages of FDM printers are their low cost, high speed and simplicity of the process. However, inter-layer distortion, layer-by-layer appearance, poor surface quality, and the limitation of thermoplastic materials are the main drawbacks of FDM printers [45-47]. Although, the application of fiber-reinforced composites has strengthened the mechanical properties of the prints, bonding between the fiber and matrix and void formation are still the challenges in printing composite parts in 3D printing [48, 49].

1.2.3. Stereo Lithography Apparatus

Stereo Lithography Apparatus (SLAs) printers use photopolymerizing resin by positioning a perforated platform just below the surface of a vat of liquid photo curable polymer

at room temperature [38]. By tracing the top slice of the object in liquid, the UV laser beam will harden the layer of photopolymer [50]. SLA can also be used in tablets drug printing, manufacturing, and hearing aid products printing [51-53].

1.2.4. Direct Metal Laser Sintering

Similar to SLS, Direct Metal Laser Sintering (DMLS), is an Additive Manufacturing (AM) process which prints objects by using a laser beam to scan a thin metallic powder layer [54]. Each layer on the platform is comprised of elongated lines of molten powder [55]. However, different from SLS, DMLS printers use uncoated pre-alloyed metal powders instead of polymers [56]. Some features in the process such as scanning speed, laser power, and hatching distance are important since they will directly result in the difference found in the products' characteristics like surface quality and porosity [57]. It is possible to produce bulk objects with a residual porosity below 0.8% by using up-to-date DMLS techniques [58]. One of the most important benefits of DMLS printers is their ability to produce complex shaped metal components directly on the printing platform [55]. Meanwhile, the specially optimized powder for DMLS printers makes it easier to operate accurately since it provides a broader processing window [59]. However, DMLS still has drawbacks such as slow build rates as well as the limitation of component size [33].

1.3. Background of topology

Topology optimization is a mathematical method for optimizing the distribution of materials in a specific region based on the given load conditions, constraints, and performance index. Topology optimization, which includes size optimization and shape optimization, is an effective method to design and determine the initial configuration of the product in the initial stage of product design.

Each component in the assembly will have extra weight unless it is topologically optimized. The extra weight means using extra materials, moving parts with higher loads, lower energy efficiency, and the cost of transporting parts. With topology application, ANSYS Mechanical can now help users design lightweight and durable components for any application. The user can easily define the target and apply various controls to ensure that the manufacturing requirements are met, while the minimum material thickness is set, and the exclusion zone is defined.

The continuum structure topological optimization design is a challenging research direction in the field of structure optimization after the size and shape optimization design. It is a higher-level size and shape optimization method and is also the most complex problem in structural optimization. In topology optimization of continuum structures, the shape boundaries, both external and internal and the number of inner holes is optimized simultaneously with respect to a predefined design objective. Traditional design processes cannot make full use of new manufacturing methods, such as additive manufacturing, which can eliminate design constraints and create new opportunities. The best component shapes are often organic and counterintuitive, and therefore require a different approach to design. Topology optimization techniques allow users to specify the location of the support points and load points on the material volume and let the software find the best shape. The models are the result of superfluous geometries removed while maintaining the original mechanical strength, which can be quickly verified as the optimal design. In addition, users can also simulate various space-related materials, such as composite materials, 3D printing polymers, and bones and tissue, to obtain more accurate results.

At present, the mainstream topological optimization methods include homogenization method [60], variable density method [61], the evolutionary structural optimization [62], level-set method [63], and bi-directional evolutionary topology optimization [64]. From those methods, the Evolutionary Structural Optimization (ESO), by reason of usability and high efficiency, has been widely accepted by engineers and architects. The ESO method was first presented in the early 1990s. By gradually removing the low-stress materials in the structure, the remaining structures eventually become the optimal one. The process of the method is simple and fast. Meanwhile, the ESO method can be used by several finite elements analysis (FEA) software, such as ABAQUS and ANSYS.

1.4. Kinematic Analysis

Calculation of multi-body system dynamics analysis includes modeling and solving the motion equations. Modeling can be divided into physical modeling and mathematical modeling. Physical modeling is the establishment of a geometric model based on a physical model. By evaluating the kinematic constraints of the geometric model, and external forces, and the torque, as well as the boundary condition, the dynamic characteristics of the physical model can be obtained.

CHAPTER 2

THEORETICAL BACKGROUND

Since the structure of soft robotics can be considered a continuum, sensing and controlling the shape of a soft robot is more challenging than in the rigid case. It is difficult to measure and also hard to use measurement equipment to control the mobility of soft robots, especially considering the effect of gravity. Hard robots can be measured for the position of each joint by forwarding kinematics with high-level accuracy. Moreover, based on the theory of rigid body kinematics, inverse kinematics also can be applied for determining the joint positions that can provide the desired position.

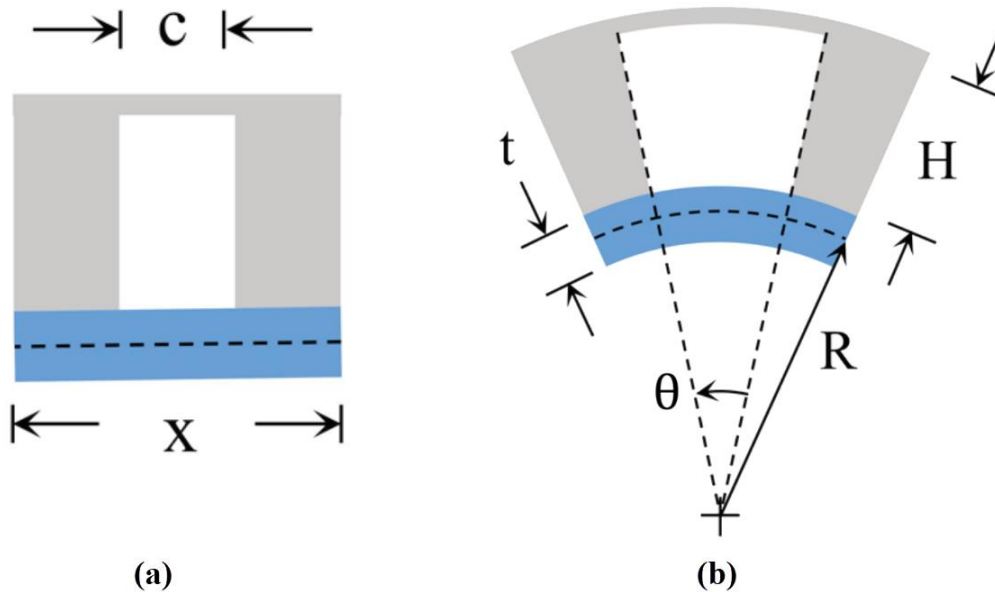


Figure 8 The Pneu-Net chamber before (a) and after (b) inflated

For example, consider the curvature κ as the control input to determine the displacement of a pneumatic actuator [65]. The positive and negative sign of the number κ determine the

bending direction: $\kappa < 0$ corresponding to the clockwise direction, and $\kappa > 0$ corresponding to the counterclockwise. The curvature κ for a soft robotic actuator can be defined as

$$\kappa = \frac{\partial \theta}{\partial s} \quad (3)$$

Where θ is the angle between the bent actuator and its original position (as shown in Figure 8(b)), and s is the arc-length parameter from the fixed or pivot point to the centerline.

The total potential energy Π in this structure:

$$\Pi = U + V_{PE} \quad (4)$$

Where U is the sum of the elastic strain energy; and V_{PE} is the potential energy. The elastic strain energy can be calculated by the bending angle and the bending moment as shown in equation (5),

$$U = \frac{1}{2} \theta M = \frac{1}{2} \frac{M^2 L}{2EI} \quad (5)$$

Also, the relation between moment and curvature can be expressed as

$$M = \kappa EI \quad (6)$$

Substituting equation (6) into equation (5), the elastic strain energy U can be written as

$$U = \frac{\kappa^2 E^2 I^2 x}{2EI} = \frac{1}{2} \kappa^2 EI x \quad (7)$$

To simplify the formula, let

$$EI = D = E \frac{wt^3}{12(1 - \mu^2)} \quad (8)$$

Where μ is Poisson's ratio; w is the weight of bending actuator; t is the thickness of the bottom layer, so that the elastic strain energy is

$$U = \frac{1}{2}D\kappa^2L \quad (9)$$

Second, we calculate the potential energy

$$V_{PE} = PV \quad (10)$$

Where P is the pressure inside, and the inside volume V can be written as

$$V \approx \frac{1}{2}\theta[(R + H)^2 - R^2]w = \frac{1}{2}\kappa c[(R + H)^2 - R^2]w \quad (11)$$

Where c is the length of chamber, shown as Figure 8(a). Since the static is equilibrium, the condition for minimum potential energy has to be met, $\frac{\partial \Pi}{\partial \kappa} = 0$

Combining the equations (9-11) into equation (4), the total potential energy can be defined as:

$$\Pi = \frac{1}{2}\kappa^2 EIx + \frac{1}{2}\kappa c[(R + H)^2 - R^2]w \quad (12)$$

Where R is the inverse of the curvature $R = \frac{1}{\kappa}$. The potential energy can be rewritten as:

$$\Pi = \frac{1}{2}\kappa^2 Dx + \frac{1}{2}\kappa cH^2w + \frac{1}{2}\kappa c \frac{2H}{\kappa} w \quad (13)$$

And, deriving κ on both sides of the equation (13),

$$\frac{\partial \Pi}{\partial \kappa} = \kappa Dx + \frac{1}{2}cH^2w = 0 \quad (14)$$

$$\kappa = -\frac{PH^2c}{2Dx}w \quad (15)$$

Substituting equation (8) into equation (15),

$$\kappa = -\frac{6(1 - \gamma^2)PH^2c}{Et^3x} \quad (16)$$

Assuming that one end of the pneumatic actuator has been fixed in order to get closer to the actual situation, and l is the length of the given actuator when it is fully extended (which

makes $\kappa = 0$). The displacement $d(\kappa)$, whose upper part of each equation represents x direction, and lower part represents y direction, can be defined as [66]

$$d(\kappa) = \begin{cases} \frac{1}{\kappa} \begin{pmatrix} \sin(\kappa s) \\ 1 - \cos(\kappa s) \end{pmatrix}, & \kappa \neq 0, \\ \begin{pmatrix} s \\ 0 \end{pmatrix}, & \kappa = 0 \end{cases} \quad (17)$$

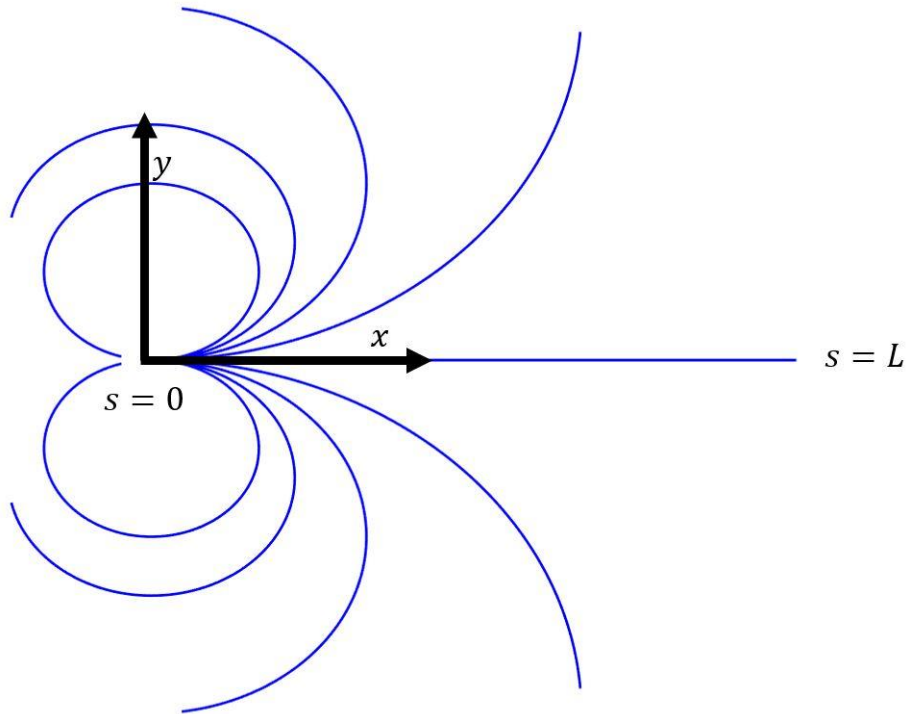


Figure 9 The range of motion of a single pneumatic actuator

To obtain a more accurate result, the model can be assumed to a cantilever with uniform load and a fixed end.

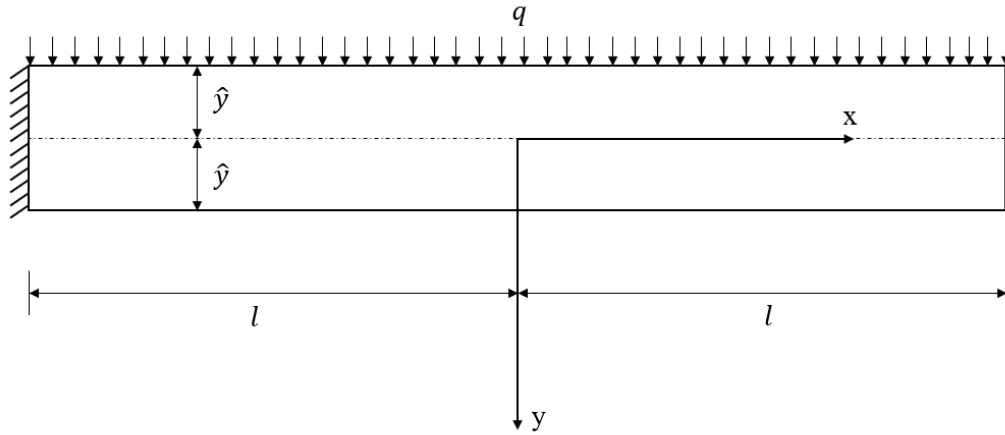


Figure 10 The schematic diagram of a cantilever beam with uniform distributed load

By analyzing the bending moment for the cantilever, an equivalent between pressure p , which is caused by injecting fluid, and load q is needed.

For the cantilever beam

$$M = \frac{1}{2}qL^2 = 2ql^2 \quad (18)$$

Where q is the uniform load on the beam, and l is the half of total beam length, which $2l = L$. Substituting equation (18) into equation (6),

$$M = \kappa EI = -\frac{PH^2c}{2L}w = \frac{1}{2}qL^2 \quad (19)$$

$$q = -\frac{PH^2cw}{L^3} \quad (20)$$

The boundary condition for the normal stress σ_y , which is caused by the load q , at the top and bottom of the beam is,

$$y = -\hat{y}: \sigma_y = -q \quad (21)$$

$$y = \hat{y}: \sigma_y = 0 \quad (22)$$

Where \hat{y} is a half of total height of cantilever beam. Since this cantilever beam is not hollow inside, the total height is the height of all solid layers. The load q does not change with x , we assume that σ_y is a function about y [67], which can be expressed as

$$\sigma_y = f(y) \quad (23)$$

Since the normal stress $\sigma_y = \frac{\partial^2 \phi}{\partial x^2}$, the stress function can be defined as

$$\phi = \frac{1}{2}x^2 f(y) + x f_1(y) + f_2(y) \quad (24)$$

where the $f(y), f_1(y), f_2(y)$ are the undetermined function with respect to y . Since ϕ is the stress function which has to satisfy the compatibility equation

$$\frac{\partial^4 \phi}{\partial x^4} + 2 \frac{\partial^4 \phi}{\partial x^2 \partial y^2} + \frac{\partial^4 \phi}{\partial y^4} = 0 \quad (25)$$

Then we obtain, that:

$$f(y) = Ay^3 + By^2 + Cy + D \quad (26)$$

$$f_1(y) = Ey^3 + Fy^2 + Gy \quad (27)$$

$$f_2(y) = -\frac{A}{10}y^5 - \frac{B}{6}y^4 + Hy^3 + Ky^2 \quad (28)$$

Where A, B, C, D, E, F, G, H and K are undetermined coefficients. Thus, the stress function should be rewritten as

$$\begin{aligned} \phi = \frac{1}{2}x^2(Ay^3 + By^2 + Cy + D) + x(Ey^3 + Fy^2 + Gy) + \left(-\frac{A}{10}y^5 - \frac{B}{6}y^4 \right. \\ \left. + Hy^3 + Ky^2\right) \end{aligned} \quad (29)$$

The stress components in two dimensions are

$$\sigma_x = \frac{\partial^2 \phi}{\partial y^2} \quad (30)$$

$$\sigma_y = \frac{\partial^2 \phi}{\partial x^2} \quad (31)$$

$$\tau_{xy} = -\frac{\partial^2 \phi}{\partial x \partial y} \quad (32)$$

Substituting equation (29) into equation (30-32),

$$\sigma_x = \frac{1}{2}x^2(6Ay + 2B) + x(6Ey + 2F) + (-2Ay^3 - 2By^2 + 6Hy + 2K) \quad (33)$$

$$\sigma_y = Ay^3 + By^2 + Cy + D \quad (34)$$

$$\tau_{xy} = -x(3Ay^2 + 2By + C) + (3Ey^2 + 2Fy + G) \quad (35)$$

According to Figure 10, the boundary conditions are given by:

$$x = l: \int_{-\hat{y}}^{\hat{y}} \sigma_x dy = 0, \int_{-\hat{y}}^{\hat{y}} \tau_{xy} dy = 0, \int_{-\hat{y}}^{\hat{y}} \sigma_x y dy = 0 \quad (36)$$

$$x = -l: \int_{-\hat{y}}^{\hat{y}} \sigma_x dy = 0, \int_{-\hat{y}}^{\hat{y}} \tau_{xy} dy = 2ql, \int_{-\hat{y}}^{\hat{y}} \sigma_x y dy = 2ql^2 \quad (37)$$

$$y = \hat{y}: \sigma_y = 0, \tau_{xy} = 0 \quad (38)$$

$$y = -\hat{y}: \sigma_y = -q, \tau_{xy} = 0 \quad (39)$$

Based on the boundary conditions, the undetermined coefficients can be calculated

$$A = -\frac{q}{4\hat{y}^3}, B = 0, C = \frac{3q}{4\hat{y}}, D = -\frac{q}{2}, E = -\frac{ql}{4\hat{y}^3}, F = 0, G = \frac{3ql}{4\hat{y}}, \quad (40)$$

$$H = -\frac{q}{20\hat{y}} - \frac{ql^2}{8\hat{y}^3}, K = 0$$

Substituting all above coefficients into stress components,

$$\sigma_x = -\frac{3q}{4\hat{y}^3}x^2y - \frac{3ql}{2\hat{y}^3}xy + \frac{q}{2\hat{y}^3}y^3 - \frac{6q}{20\hat{y}} - \frac{6ql^2}{8\hat{y}^3}y \quad (41)$$

$$\sigma_y = -\frac{q}{4\hat{y}^3}y^3 + \frac{3q}{4\hat{y}}y - \frac{q}{2} \quad (42)$$

$$\tau_{xy} = \frac{3q}{4\hat{y}^3} xy^2 - \frac{3q}{4\hat{y}} x - \frac{ql}{4\hat{y}^3} y^2 + \frac{3ql}{4\hat{y}} \quad (43)$$

Substituting equation (41(43) into Hooke's Law, the equation (44(46) in a two-dimensional plane, define the normal and shear strain components as:

$$\varepsilon_x = \frac{1}{E} (\sigma_x - \mu\sigma_y) \quad (44)$$

$$= \frac{1}{E} \left[\left(\frac{q}{2\hat{y}^3} + \frac{\mu q}{4\hat{y}^3} \right) y^3 - \left(\frac{3\mu q}{4\hat{y}} + \frac{3ql^3}{4\hat{y}^3} \right) y - \frac{3q}{4\hat{y}^3} x^2 y - \frac{3ql}{2\hat{y}^3} xy + \frac{\mu q}{2} \right]$$

$$\varepsilon_y = \frac{1}{E} (\sigma_y - \mu\sigma_x) \quad (45)$$

$$= \frac{1}{E} \left[\left(\frac{-q - 2\mu q}{4\hat{y}^3} \right) y^3 + \left(\frac{3q}{4\hat{y}} + \frac{3\mu ql^2}{4\hat{y}^3} \right) y + \frac{3\mu q}{4\hat{y}^3} x^2 y - \frac{3\mu ql}{2\hat{y}^3} xy + \left(\frac{3\mu q}{10\hat{y}} - \frac{q}{2} \right) \right]$$

$$\gamma_{xy} = \frac{2(1+\mu)}{E} \tau_{xy} = \frac{2(1+\mu)}{E} \left(\frac{3q}{4\hat{y}^3} xy^2 - \frac{3q}{4\hat{y}} x - \frac{ql}{4\hat{y}^3} y^2 + \frac{3ql}{4\hat{y}} \right) \quad (46)$$

The deformation also can be calculated by derivating the normal strain equations below,

$$\varepsilon_x = \frac{\partial u}{\partial x}, \varepsilon_y = \frac{\partial v}{\partial y} \quad (47)$$

$$u = \frac{1}{E} \left[\left(\frac{q}{2\hat{y}^3} + \frac{\mu q}{4\hat{y}^3} \right) y^3 x - \left(\frac{3\mu q}{4\hat{y}} + \frac{3ql^3}{4\hat{y}^3} \right) yx - \frac{q}{4\hat{y}^3} x^3 y - \frac{3ql}{4\hat{y}^3} x^2 y + \frac{\mu q}{2} x + f_3(y) \right] \quad (48)$$

$$v = \frac{1}{E} \left[\left(\frac{-q - 2\mu q}{16\hat{y}^3} \right) y^4 + \left(\frac{3q}{8\hat{y}} + \frac{3\mu ql^2}{8\hat{y}^3} \right) y^2 + \frac{3\mu q}{8\hat{y}^3} x^2 y^2 - \frac{3\mu ql}{4\hat{y}^3} x y^2 + \left(\frac{3\mu q}{10\hat{y}} - \frac{q}{2} \right) y + f_4(x) \right] \quad (49)$$

Where the u and v is deformation in x and y , respectively. Since the shear strain γ_{xy} should follow the equation below,

$$\gamma_{xy} = \frac{\partial u}{\partial y} + \frac{\partial v}{\partial x} \quad (50)$$

Substituting equation (48) and (49) into equation (50), and arranging x and y on both sides of the equation,

$$\begin{aligned} -\frac{3q}{4\hat{y}^3} \left(\frac{x^3}{3} + lx^2 + l^2x \right) + \frac{3q}{20\hat{y}} [(8 + 5\mu)x + 10l(\mu + 1)] + \frac{df_4(x)}{dx} \\ = \frac{3(2 + \mu)ql}{4\hat{y}^3} y^2 - \frac{df_3(y)}{dy} \end{aligned} \quad (51)$$

Since the left side is a function of x , and the right side is a function of y , in order to balance the equation, each side should be equal to a constant. A constant N is assumed to equal both sides, and equation (51) can be expressed as

$$-\frac{3q}{4\hat{y}^3} \left(\frac{x^3}{3} + lx^2 + l^2x \right) + \frac{3q}{20\hat{y}} (8 + 5\mu)x + \frac{3q}{2\hat{y}} l(\mu + 1) + \frac{df_4(x)}{dx} = N \quad (52)$$

$$\frac{3(2 + \mu)ql}{4\hat{y}^3} y^2 - \frac{df_3(y)}{dy} = N \quad (53)$$

Then the function $f_3(y)$, and $f_4(x)$ can be expressed, by integrating the equation above,

as

$$f_3(y) = \frac{(2 + \mu)ql}{4\hat{y}^3} y^3 - Ny + u_0 \quad (54)$$

$$f_4(x) = Nx + \frac{3q}{4\hat{y}^3} \left(\frac{x^4}{12} + \frac{lx^3}{3} + \frac{l^2x^2}{2} \right) - \frac{3q}{10\hat{y}} (8 + 5\mu)x^2 - \frac{3q}{2\hat{y}} l(\mu + 1)x + v_0 \quad (55)$$

Where u_0 and v_0 are undetermined constants. Substituting equation (54) and (55) into displacement equations, the equation (48) and (49) result in the following expressions:

$$u = \frac{1}{E} \left[\left(\frac{q}{2\hat{y}^3} + \frac{\mu q}{4\hat{y}^3} \right) y^3 x - \left(\frac{3\mu q}{4\hat{y}} + \frac{3ql^3}{4\hat{y}^3} \right) yx - \frac{q}{4\hat{y}^3} x^3 y - \frac{3ql}{4\hat{y}^3} x^2 y + \frac{\mu q}{2} x + \frac{(2 + \mu)ql}{4\hat{y}^3} y^3 - Ny + u_0 \right] \quad (56)$$

$$v = \frac{1}{E} \left[\left(\frac{-q - 2\mu q}{16\hat{y}^3} \right) y^4 + \left(\frac{3q}{8\hat{y}} + \frac{3\mu ql^2}{8\hat{y}^3} \right) y^2 + \frac{3\mu q}{8\hat{y}^3} x^2 y^2 - \frac{3\mu ql}{4\hat{y}^3} xy^2 + \left(\frac{3\mu q}{10\hat{y}} - \frac{q}{2} \right) y + Nx + \frac{3q}{4\hat{y}^3} \left(\frac{x^4}{12} + \frac{lx^3}{3} + \frac{l^2x^2}{2} \right) - \frac{3q}{10\hat{y}} (8 + 5\mu)x^2 - \frac{3q}{2\hat{y}} l(\mu + 1)x + v_0 \right] \quad (57)$$

To solve those polynomials, it is considered that only the midpoint portion of the fixed end is absolutely fixed [67]. Therefore, the boundary conditions are considered as:

$$x = -l, y = 0: u = 0, v = 0, \frac{\partial v}{\partial x} = 0 \quad (58)$$

Based on the above, the undetermined coefficients, u_0 , v_0 , and N can be calculated as:

$$u_0 = \frac{\mu ql}{2} \quad (59)$$

$$v_0 = \frac{ql^4}{16\hat{y}^3} - \frac{(14 + 3\mu)ql^2}{2\hat{y}} \quad (60)$$

$$N = \frac{ql^3}{4\hat{y}^3} - \frac{(33 + 15\mu)ql}{10\hat{y}} \quad (61)$$

Then the displacement of the cantilever can be expressed as

$$u = \frac{1}{E} \left[\left(\frac{q}{2\hat{y}^3} + \frac{\mu q}{4\hat{y}^3} \right) y^3 x - \left(\frac{3\mu q}{4\hat{y}} + \frac{3ql^3}{4\hat{y}^3} \right) yx - \frac{q}{4\hat{y}^3} x^3 y - \frac{3ql}{4\hat{y}^3} x^2 y + \frac{\mu q}{2} x \right. \\ \left. + \frac{(2 + \mu)ql}{4\hat{y}^3} y^3 - \frac{ql^3}{4\hat{y}^3} y + \frac{(33 + 15\mu)ql}{10\hat{y}} y + \frac{\mu ql}{2} \right] \quad (62)$$

$$v = \frac{1}{E} \left[\left(\frac{-q - 2\mu q}{16\hat{y}^3} \right) y^4 + \left(\frac{3q}{8\hat{y}} + \frac{3\mu ql^2}{8\hat{y}^3} \right) y^2 + \frac{3\mu q}{8\hat{y}^3} x^2 y^2 - \frac{3\mu ql}{4\hat{y}^3} x y^2 \right. \\ \left. + \left(\frac{3\mu q}{10\hat{y}} - \frac{q}{2} \right) y + \frac{ql^3}{4\hat{y}^3} x - \frac{(33 + 15\mu)ql}{10\hat{y}} x \right. \\ \left. + \frac{3q}{4\hat{y}^3} \left(\frac{x^4}{12} + \frac{lx^3}{3} + \frac{l^2 x^2}{2} \right) - \frac{3q}{10\hat{y}} (8 + 5\mu)x^2 - \frac{3q}{2\hat{y}} l(\mu + 1)x \right. \\ \left. + \frac{ql^4}{16\hat{y}^3} - \frac{(14 + 3\mu)ql^2}{2\hat{y}} \right] \quad (63)$$

The bottom layer is the target layer for observation, and the curvature at the bottom layer is a favorable parameter for calculating the position after deformation by using equation (17). To calculate the curvature of the bottom layer, the $y = \hat{y}$ will be substituted. The curvature at bottom layer of cantilever beam is

$$\kappa_{opt} = \frac{d^2 v}{dx^2} = \frac{1}{E} \left[\frac{3\mu q}{4\hat{y}} + \frac{3q}{4\hat{y}^3} (x^2 + 2lx + l^2) - \frac{3q(8 + 5\mu)}{5\hat{y}} \right] \quad (64)$$

CHAPTER 3

DESIGN AND MODELING

3.1. Design

Soft robots can be designed similar to a prototypical soft actuator, muscle. Since muscle is a complicated soft tissue which is able to shrink accurately by animal control, the total functions of animal muscle cannot be replicated by currently existing technology [68]. However, these actuators have similar functions to natural muscles, like a length-load, and can react to human operation very quickly, which can be replicated through numerical methods like finite element analysis.

The pneumatic network (Pneu-Net) bending actuator, which has several chambers whose thickness are not the same on each surface, behaves like a bladder, is used in this thesis as a prototype for design modeling and fabrication purpose. When chambers inside are inflated, all the internal empty spaces of the Pneu-Net actuator swell. At the meantime, a thin inextensible layer which is set under the bottom layer prevents the bottom layer from extending. The larger deformation of the upper actuator and the smaller deformation of the lower constitute a bending moment. Our current design uses a model made up from 14 chambers, shown as Figure 11. The walls between every two adjacent chambers are thinner than the other walls in order to realize larger deformation when subjected to high pressure. The bottom of this model embeds an inextensible layer to limit the movement and deformation. All the chambers are connected by a through-channel, which ensures that once the compressed air is injected from the gas injection port, the pressure of the entire inner chambers is equally applied.

Air is a reasonable choice for our injection material as it is not difficult to restore since it is compressible. Moreover, it does not increase the weight of soft robots when filled to full. Also, the viscosity of air is low; thus, it will quickly flow into the whole inner space to uniformize the pressure in every point inside.

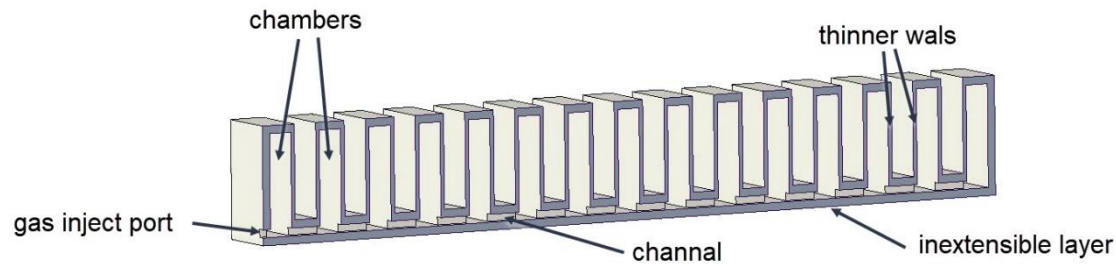


Figure 11 3D Sketch for Pneu-Net actuator by Creo 4.0

3.2. Traditional casting fabrication

Conventional manufacturing of Pneu-Net bending actuators typically requires the use of a casting method. In addition to modeling the bending actuator shape, this method also requires modeling and fabrication of the mold of the actuator to implement the casting (Figure 12) [69]. As the picture shows, the process of casting a pneumatic actuator is time-consuming. First, the elastomer must be mixed and poured into the mold until the upper body mold fills completely. Then, filling of half of the base mold frame has to be done in order to put a sheet of inextensible material, such as paper, as a strain-limiting layer. Second, when both parts become solid, the main body part needs to be demolded. The third step is to fill the remaining half of the base mold with the uncured elastomer. Before the elastomer cures, bonding of the upper body to the base has to occur. When all the elastomer material is cured, the final actuator can be demolded.

As described in the previous section, a Pneu-Net actuator consists essentially of two parts: the upper body contains a chamber that will expand when the actuator is inflated and a

bottom layer that contains the strain limiting material such as paper layer. These two parts must be molded separately and then glued together. Thus, an additional process for pouring into molds is unavoidable.

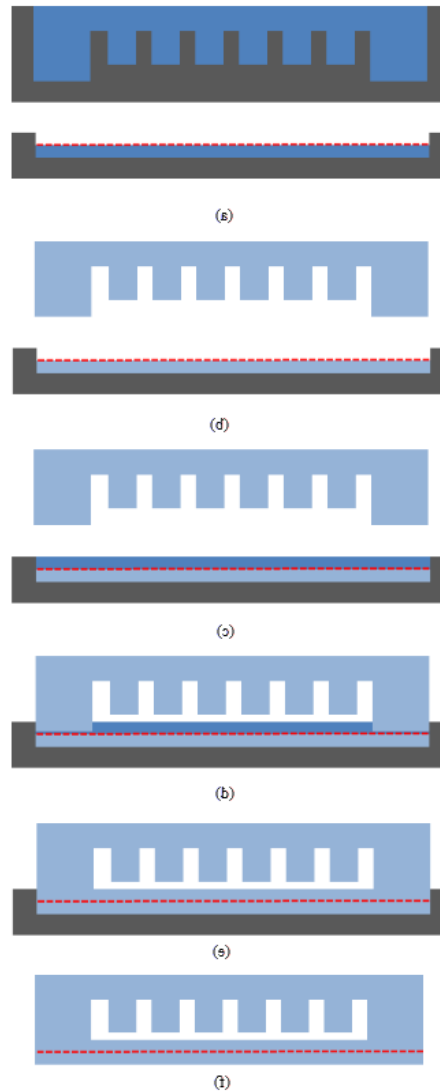


Figure 12 Processing overview for traditional pneumatic bending actuators fabrication

However, as printing technology continues to advance, it is not impossible to directly print a pneumatic bending actuator with hollow chambers. Details on direct printing of the Pneu-Net will be detailed in subsequent sections.

CHAPTER 4

SIMULATION

4.1. Creating geometry model

To simulate the Pneu-Net model with ANSYS, creating a 3D geometry model is a necessary step. CAD software, Creo 4.0, was chosen for sketching and 3D modeling. The three views of the Pneu-Net actuator are shown in Figure 13. Our Pneu-Net bending actuator is based on previous works [29, 70, 71]. By changing original Pneu-Net parameters, the new design includes 14 chambers and a channel through one end to the last chamber in order to fill the entire actuator when pressurized.

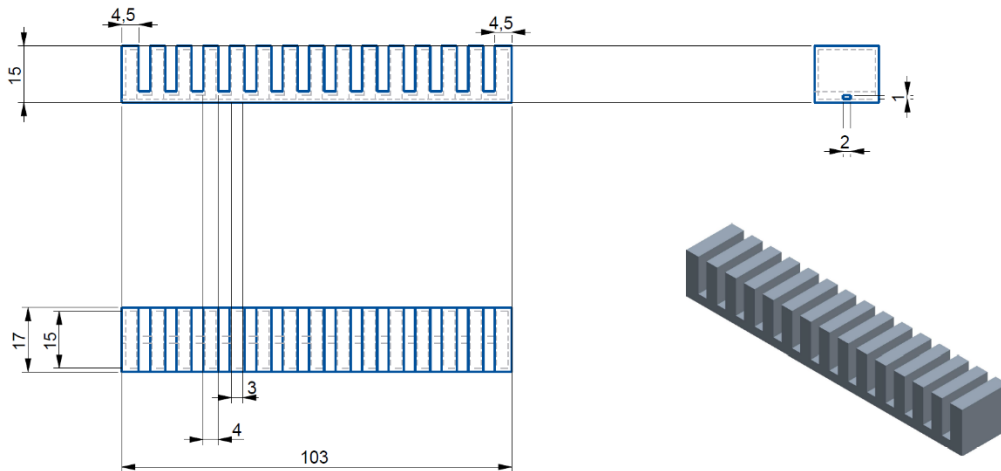


Figure 13 Three views and isometric view of Pneu-Net actuator (Units: mm)

4.2. Simulation in ANSYS with linear properties of material

After the 3D model was created, it was imported into finite element analysis software, ANSYS. In the process of 3D printing, NinjaFlex material was chosen as the main material of our Pneu-Net bending actuator. The properties of the material are shown in Table 2.

Table 2 the properties of NinjaFlex [72]

Density	1190kg/m³
Young's modulus	12MPa
Poisson's ratio	0.48[73]
Bulk Modulus	1 * 10 ⁸ Pa
Shear Modulus	4.0541 * 10 ⁶ Pa
Tensile Yield Strength	4 MPa
Tensile Ultimate Strength	26 MPa
Elongation as Yield	65%
Elongation at Break	660%
Toughness	82.7 * 10 ⁶ m * N/m ³

For the realization of the inextensible bottom layer, a layer, with thickness of 0.5 mm, is embedded under the bottom layer. The layer is set to be orthotropic so that in the longitudinal axial direction the bottom layer cannot be extended, but it is still flexible and bendable.

The default element size was set to 1 mm and the meshing method was defined as Hex dominant to generate a hexagonal element mesh. In the final mesh statistics, there were 145,978 nodes and 51,509 elements, shown as Figure 14.

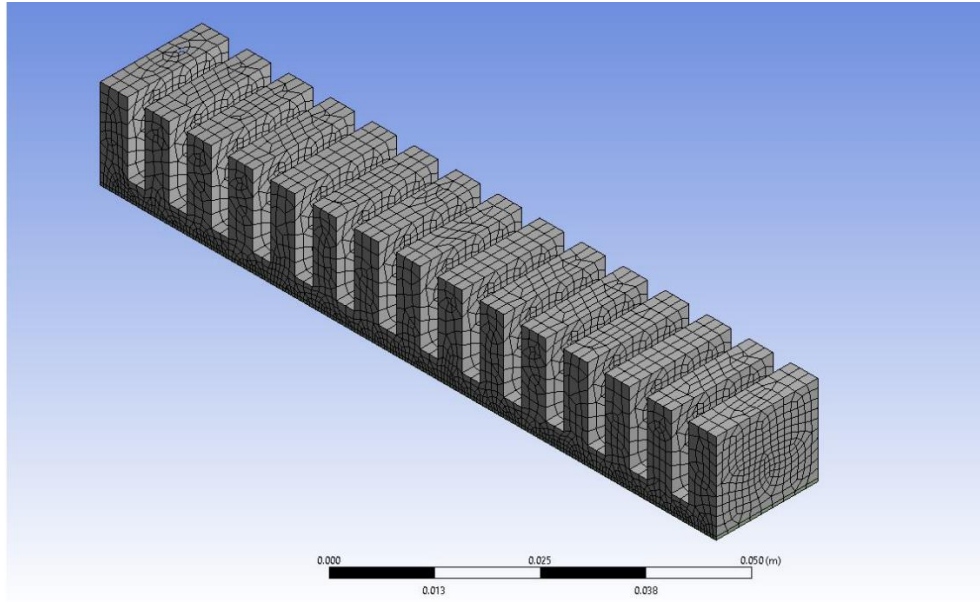


Figure 14 Schematic diagram of meshing in ANSYS

By collecting 11 groups of data for different pressure values at the inlet relation between pressure and displacement is established (this is shown in Table 5). The displacement data is collected by observing the end of bottom layer which was set as the “monitor edge” as a consistent observation (Figure 15 The place of monitor edge).

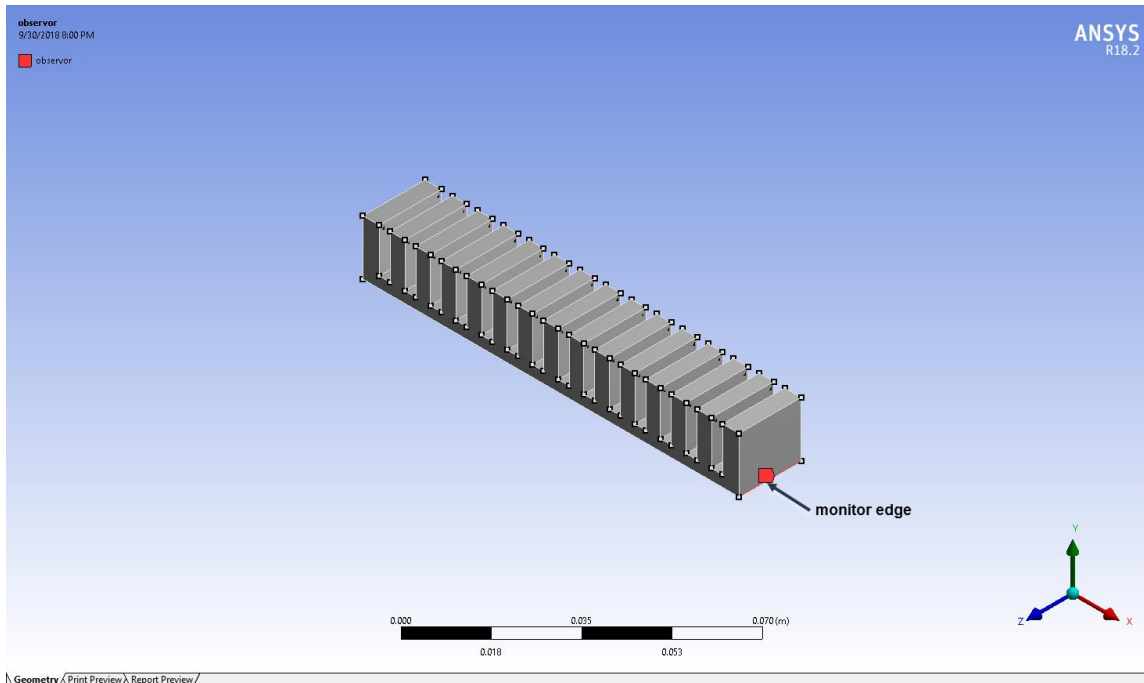


Figure 15 The place of monitor edge

As seen in Figure 16-18, the displacement in x axis increases with pressure until this reaches 130,000 Pa. When pressurizing over than 130,000 Pa, the Pneu-Net bending actuator attains a semicircle trajectory. After this value, if the pressure increases, the displacement in x direction decreases and starts getting actuator closer to the y-axis. Also, for the pressure between 130,000 to 150,000 Pa, the x directional displacement is over than 0.103m, which is the original length of Pneu-Net bending actuator. This data means that the bending actuator has been become a semicircle in the x-y plane. From 200,000 Pa to 250,000 Pa, the displacement in the x direction starts to increase. This phenomenon demonstrates the bending actuator has become three quarters of a circle.

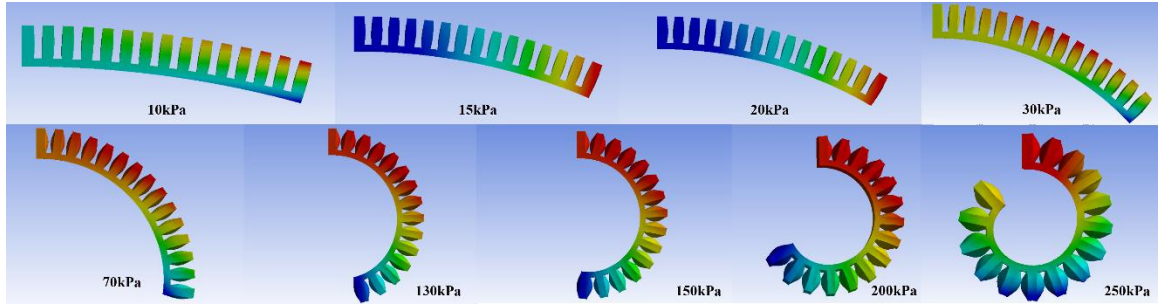


Figure 16 The linear material properties Simulation results under different pressures

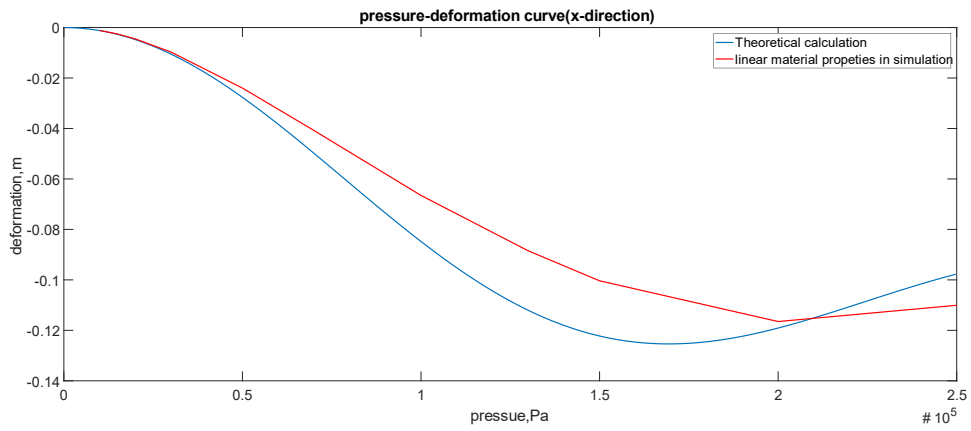


Figure 17 The pressure-deformation curve comparison chart of linear material properties Simulation results under different pressures in x-direction

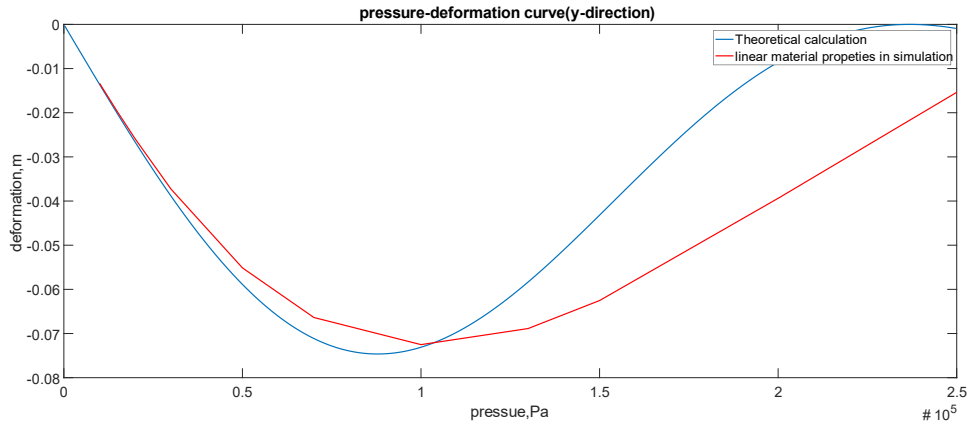


Figure 18 The pressure-deformation curve comparison chart of linear material properties Simulation results under different pressures in y-direction

4.3. Simulation in ANSYS with nonlinear properties of material

Soft actuators are typically made from hyperelastic materials, such as silicone rubber, and these materials have nonlinear properties. For this reason, an adjustment to the FEA model was made in order to include this hyperelastic behavior in the material.

Neo-Hookean model

The neo-Hookean model was proposed by Ronald Rivlin in 1948. This type of material is a hyperelastic material. Comparing with linear elastic materials, neo-Hookean materials have a nonlinear relationship in the stress-strain curve (see Figure 19) [74]. The stress-strain curve has a linear behavior at the beginning stage. However, after the linear stage, the stress-strain curve becomes smoother with increasing stress.

Mooney-Rivlin model

In 1948, Mooney and Rivlin introduced a new hyperelastic material model which was named after them. The Mooney-Rivlin material model is applied to characterize materials which

undergo large strains [75]. The strain energy density function for an incompressible Mooney-Rivlin material is [76, 77]

$$W = C_1(\bar{I}_1 - 3) + C_2(\bar{I}_2 - 3) \quad (65)$$

Where C_1 and C_2 are material constants, and \bar{I}_1 and \bar{I}_2 are the first and second deviatoric strain invariant respectively. It is worth noting that the model can become neo-Hookean model when $C_2 = 0$.

Yeoh model

The Yeoh hyperelastic material model is a phenomenological model for the deformation of nearly incompressible and nonlinear elastic materials [78]. The model is based on Rivlin's observation that the elastic properties of rubber may be described using a strain energy density function which is a power series for the strain invariants I_1, I_2, I_3 [79].

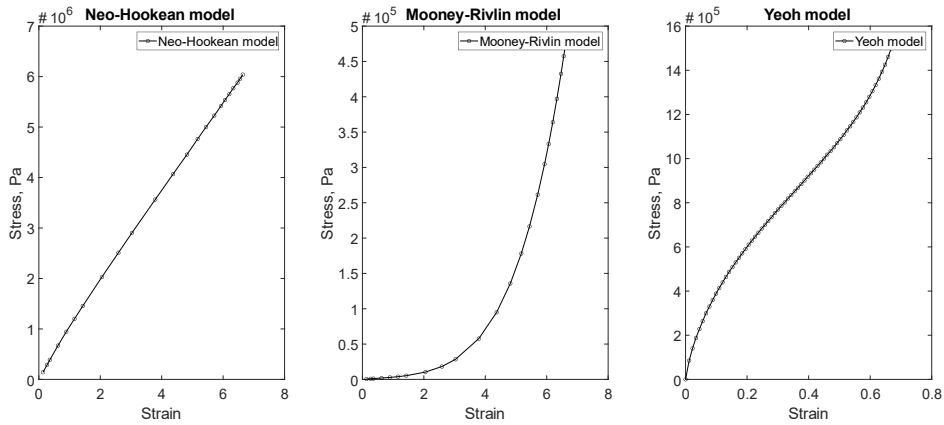


Figure 19 Stress–strain curves for various hyperelastic material models.

Based on previous works [80], the NinjaFlex material is more suitable to the Yeoh hyperelastic model. The authors also provide the ANSYS hyperelastic parameters, which are shown in Table 3.

Table 3 Yeoh hyperelastic parameters in ANSYS

C_{10}	C_{20}	C_{30}
1.653	0.0324	0.000468

Based on the revised material properties, a new simulation was setup. The new model is similar to the old one, but the material of the main body was changed to fit a hyperelastic material. The embedded layer still uses the linear material because it is only used for limiting the axial extension. The thickness of inextensible layer is small enough so that the effect on bending can be ignored. Table 6 shows 11 groups of data collected from the ANSYS simulation result.

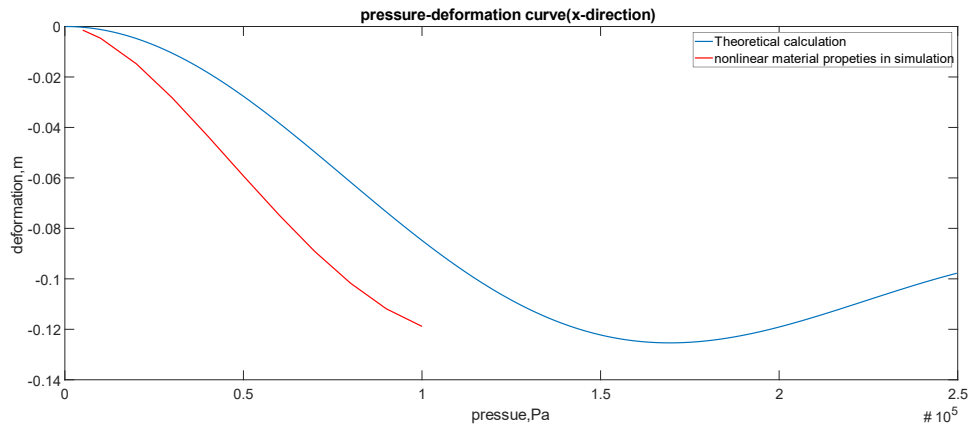


Figure 20 The Pressure-deformation comparison chart of nonlinear material properties Simulation results under different pressures in x-direction

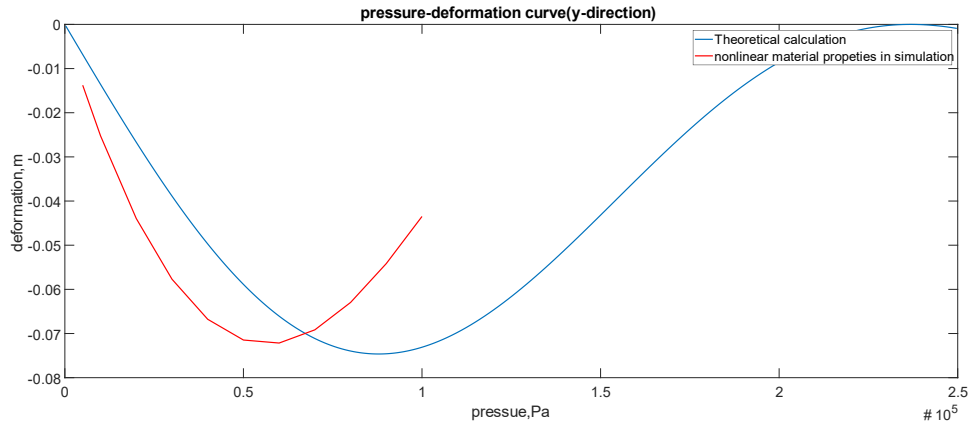


Figure 21 The Pressure-deformation comparison chart of nonlinear material properties Simulation results under different pressures in y-direction

As Figure 20-22 show, in the beginning stage of pressurizing, pressure values from 5000 to 60000 Pa, the displacement of monitor edge in both x-axis and y-axis decreased. As the pressure increases, the displacement in x direction still decreases. However, the displacement in y direction increases since the bending actuator starts becoming a circle.

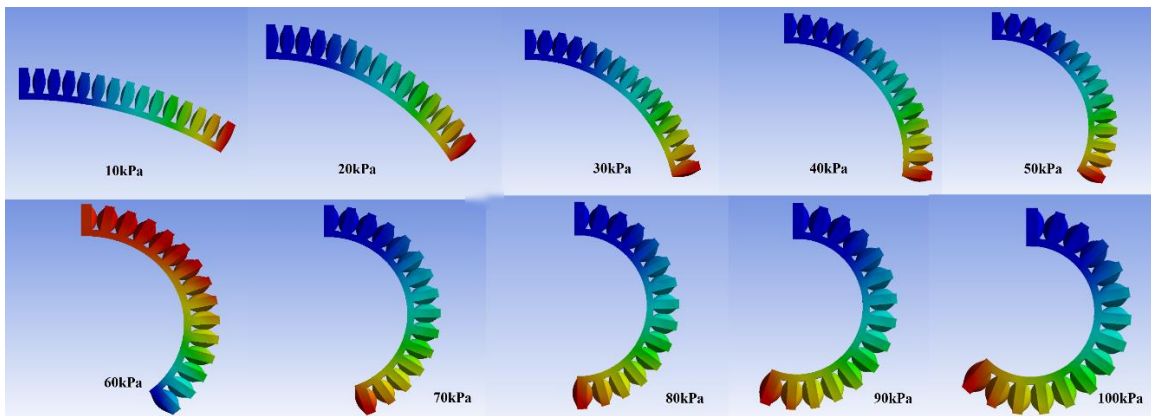


Figure 22 The nonlinear material properties Simulation results under different pressures

Through MATLAB, we can compare the differences between the two groups of data, linear material and nonlinear material, as well as the theoretical data. As Figure 23 and Figure 24 show, the linear material simulation matches the theoretical data better.

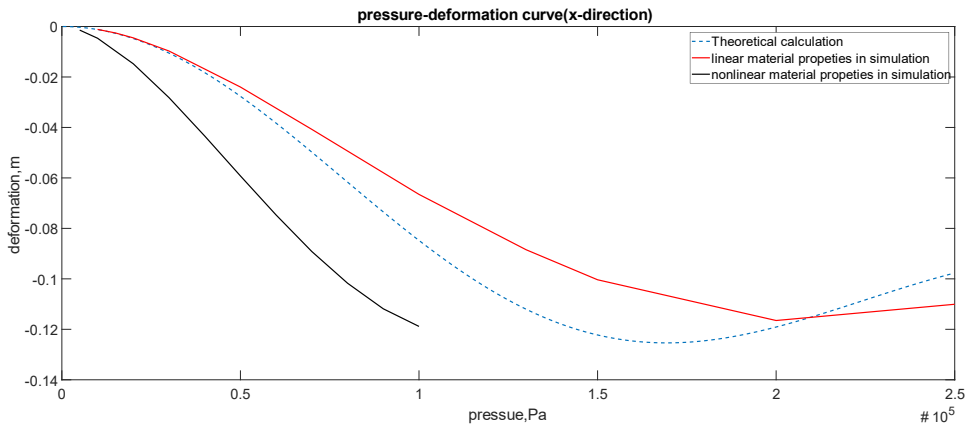


Figure 23 Comparison between linear, nonlinear material properties simulation and theoretical in x-direction

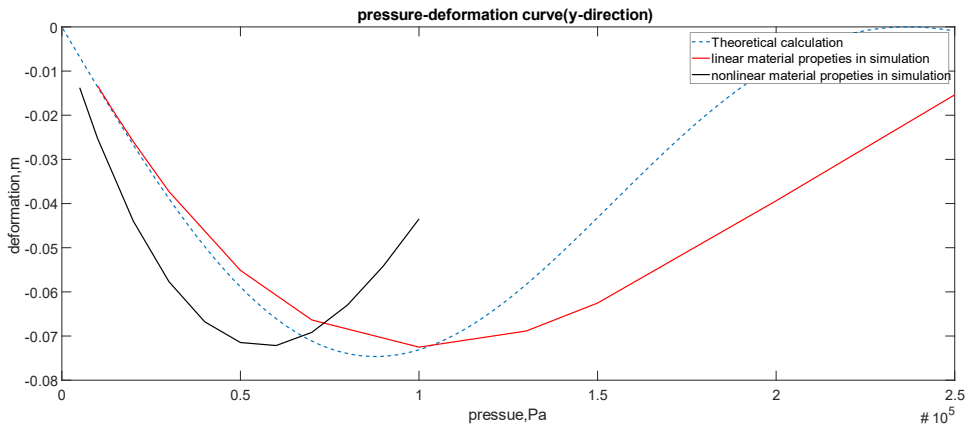


Figure 24 Comparison between linear, nonlinear material properties simulation and theoretical in y-direction

CHAPTER 5

3D PRINTING PRODUCT EXPERIMENT

For the process of 3D printing, a material called NinjaFlex was chosen. The printer is a Folger Tech Ft-5 R2 Large scale 3D Printer, which is shown in Figure 25. The overall size of the printer is $740 \times 500 \times 540$ mm and has $300 \times 300 \times 400$ mm building area which satisfies our requirement of model size. The power of the printer is 480W, which can provide a maximum of 245°C for the extruder temperature and 120°C for the building plate temperature.

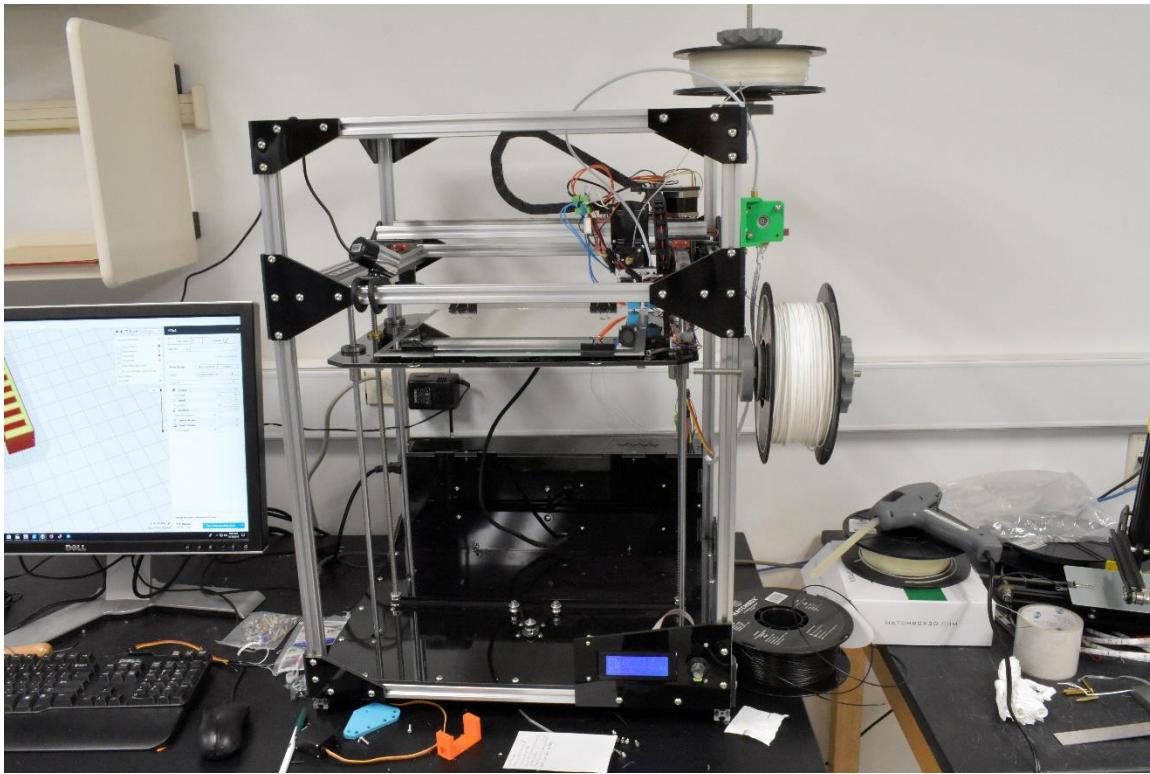


Figure 25 Folger Tech Ft-5 R2 large scale 3D Printer

The printer settings are controlled by the software, Cura, which generates G-code lines from the slicer application. Moreover, G-code can also be changed directly which is also a good method to achieve a desired setting. It is effective but time consuming.

For the experiment, the extruder temperature was set around 230°C and it depends on material properties. If the temperature is lower than 220°C, the melt material cannot stick as dragging phenomenon occurs (see Figure 26). The dragging, also called oozing, happens when the nozzle sometimes “oozes” filament while traveling and this sticks to the surface of the printing product. If the temperature is higher than 240°C, the extruder may scorch the layers which were already printed and had cooled down (see Figure 27). The color of the scorched layer becomes brown, and the stiffness of the overall printed material is increased; therefore, this would affect subsequent experiment results directly. The building plate temperature is also a sensitive parameter for 3D printing and 80°C is a good one for NinjaFlex based on several printing attempts.



Figure 26 Finished product after dragging phenomenon



Figure 27 Finished product after scorch phenomenon

The retraction is a movement which is able to pull back the filament that has entered the extruder by a small distance. It is a very important parameter in order to achieve high quality prints. An over-low retraction distance may cause the material to deposit on the part's exterior faces. Dragging and threads between each layer may happen when the parameter is set too high. For example, our first failure printing product had a lot of threads and breakages on the vertical walls. We found that the problem was the distance of retraction being set too large (about 12 mm). After reducing the retraction distance to 1 mm, the new results were acceptable. Every edge is measured by a Vernier caliper to collect as much data as possible. Those edge lengths were used to calculate the error of model size. The results are shown in Table 4, and Figure 28 shows the coordinate system of the printing area.

Table 4 The design length and actual length for each direction of printed model

x-axis direction	Designed value, mm	3
	Average measured, mm	3.162143
	Relative error	0.054048
y-axis direction	Designed value, mm	4
	Average measured, mm	4.011538
	Relative error	0.002885
z-axis direction	Designed value, mm	17
	Average measured, mm	16.94533
	Relative error	-0.00322

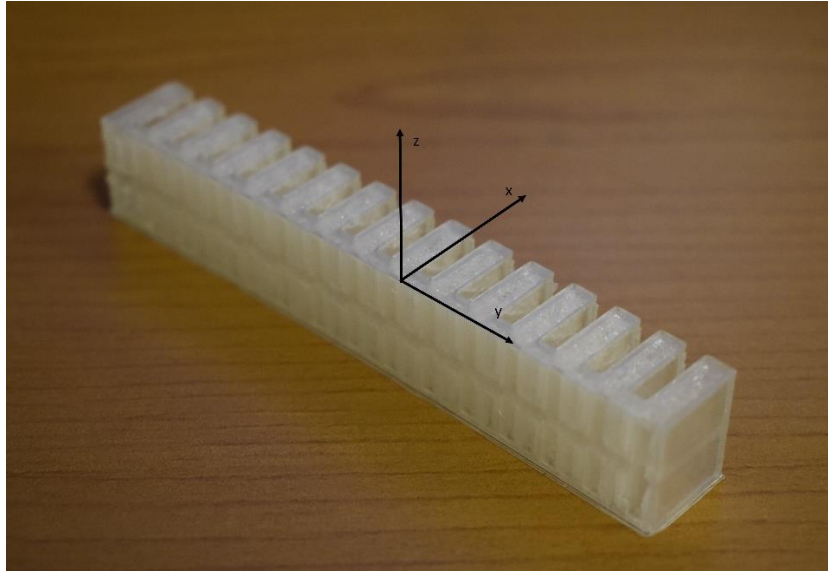


Figure 28 The coordinate system of printing area

5.1. Optimization of 3D printing setting

For the first printing attempts, the basic 3D printing settings were tentative. To optimize the printing quality, it was necessary to fine adjust each main printing parameter. Four varieties were chosen for this experiment, printing speed, retraction distance, flow, and extruder temperature.

The parameter flow of 3D printing is a percentage of melted filament that is extruded from the heated nozzle. The default setting for most situations is 100%. However, the ability to leakproof the 3D printed pneumatical actuator is extremely important. Thus, increasing flow percentage is necessary to avoid any pores or holes, and breakages, through lack of adhesion between two adjacent layers. On the other hand, a higher percentage of flow may cause overflow, which means too much melted filament is extruded. Abundant melted material cannot

cool down in time, and it spreads to other adjacent layers, or nether layers, dropping the printing accuracy of the part.

To accurately set the flow parameter, we chose five flow percentages, 100%, 105%, 110%, 115%, and 120%. The printed model was an extremely small cube (2.5mm × 2.5mm × 2.5mm) in order to generate a very thin brim. A brim is a base layer attached to the printed model. It is usually used to assure that the first layer can successfully stick onto the build plate. For this experiment, the brim width was set to 7 mm, which translated into a circle with a radius of 5 mm. The printed product is shown in Figure 29.

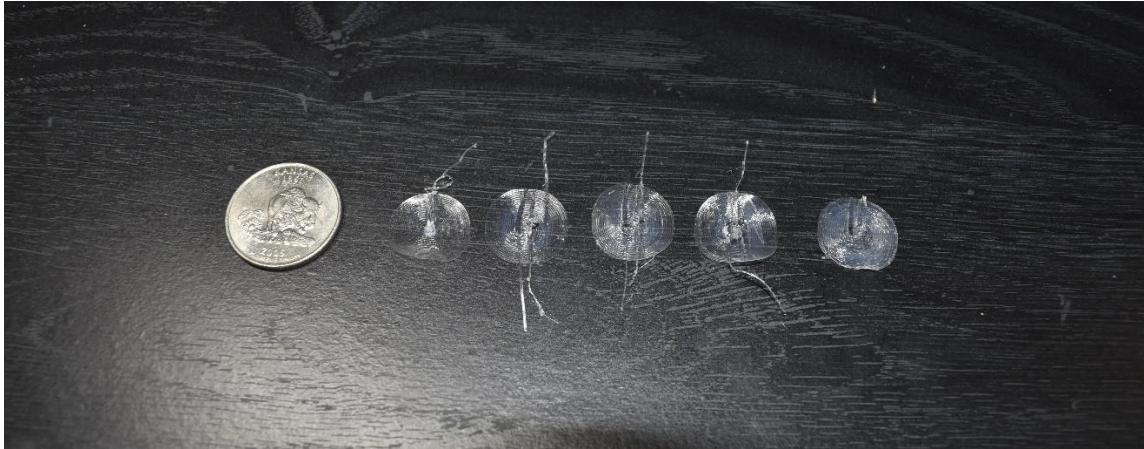


Figure 29 The printed “flow” samples (from left to right:100%, 105%, 110%, 115%, 120%)

After the “flow” samples were printed, the next step was to observe the texture, bubbles, and flaws by optical microscopy (as shown in Figure 30).

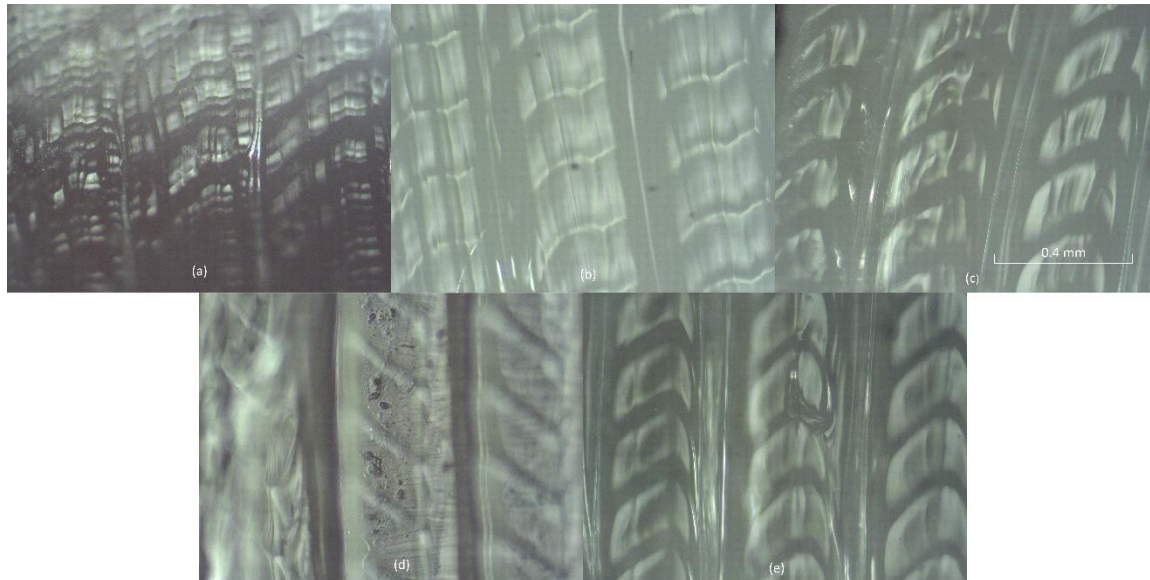


Figure 30 Microscopy images for different flow settings at the samples' edges.

The texture at the center of the flow samples is somewhat different from the texture at the samples edge, shown as Figure 31. When the 3D Printer prints the brim, the movement trail is like a swirling from the outside to the inside. When the nozzle starts to extrude melted filament, the temperature difference causes the molten filament to solidify quickly. This fast cooling process also causes some of the internal bubbles to have no time to slowly surface. In addition, the vacancies formed by the floating bubbles may not be filled by the surrounding materials in time due to rapid cooling, thereby forming flaws. In the image of the center of the brim, we can see that the result of the whole texture is greatly improved. However, for the case of 115% and 120% flow, another problem followed: overflow. The molten filament is not solidified in time. Meanwhile, in an unsolidified filament, it flows to both sides of the path. Thus, there is an

overflow. When printing only one layer, overflow does not have a big impact on print quality. However, in multiple layers printing, this error may cause problems and defects in the side walls.



Figure 31 Microscopy images for different flow settings at the samples' center.

CHAPTER 6

EXPERIMENT

To verify the theoretical and simulation results, an experiment was designed. The goal of the experiment is to obtain the displacement of the free end of the pneumatic bending actuator. To achieve this purpose, a set of experimental equipment was assembled as shown in Figure 32. During the experiment, a large column syringe was used to inject air into the pneumatic bending actuator, which was directly printed by 3D printer. A manometer was used for measuring the inner pressure of the actuator. Considering that high pressure may cause some deformation in the connecting tubing, all connecting tubing was made of hard plastic to minimize any error in the experiment. Finally, tee tubing is used for connecting each component. An indispensable step was fixing the inlet side of the bending actuator to obtain experiment data with the same boundary condition as the simulation and theoretical analysis. However, a leaking test is necessary for this experiment because every leaking point will cause the pressure to be instable and the results would be skewed.

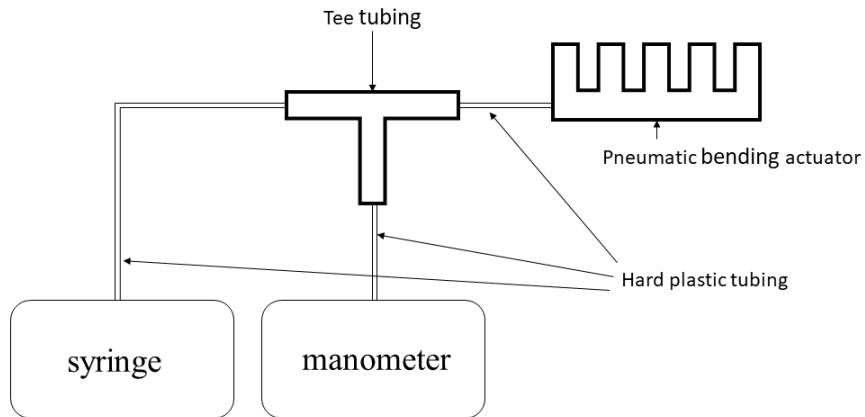


Figure 32 The schematic diagram of experiment equipment

For the entire duration of the experiment, the pneumatic bending actuator is inflated by pumping the syringe. The pressure shown on the screen of the manometer is the control indicator of the inner pressure. The bending motion, which is shown in Figure 33, of the actuator is recorded by marking on grid paper. Each pressure level was recorded for several tests to assure the accuracy of our experimental data.

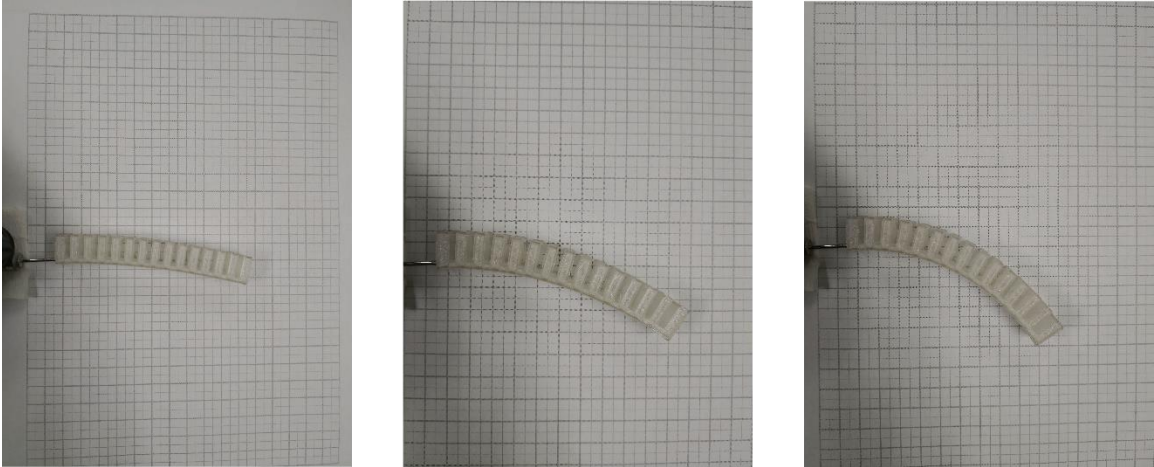


Figure 33 The process of bending for Pneu-Net actuator

After collecting all of the experiment data, a comparison between experiment data and the data from simulation, for linear and nonlinear material properties, and the mathematical model was created. This comparison is shown in Figure 34 and Figure 35. Comparing the three displacement lines for each axis, the experiment data appears to correlate well to the linear material simulation. The nonlinear material properties simulation has a similar tendency with the experiment, but the error for each test point is larger than the error between the linear material properties simulation and experiment.

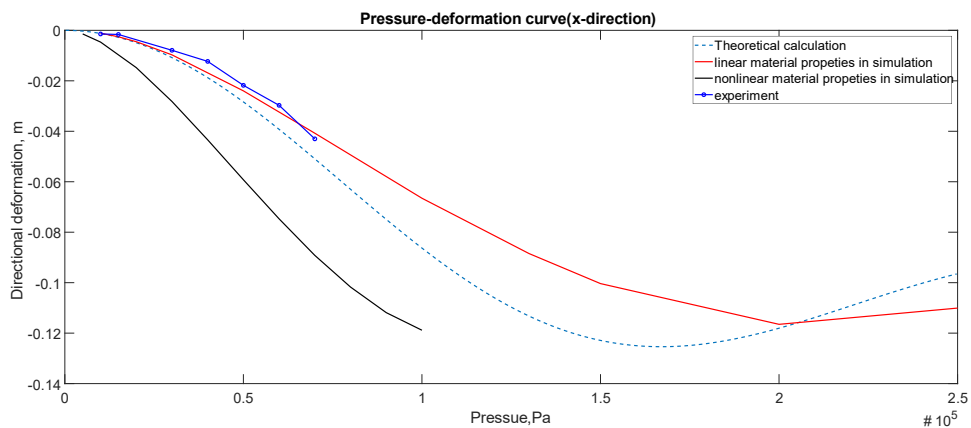


Figure 34 Comparison between experiment results, simulation, and theoretical in x-direction

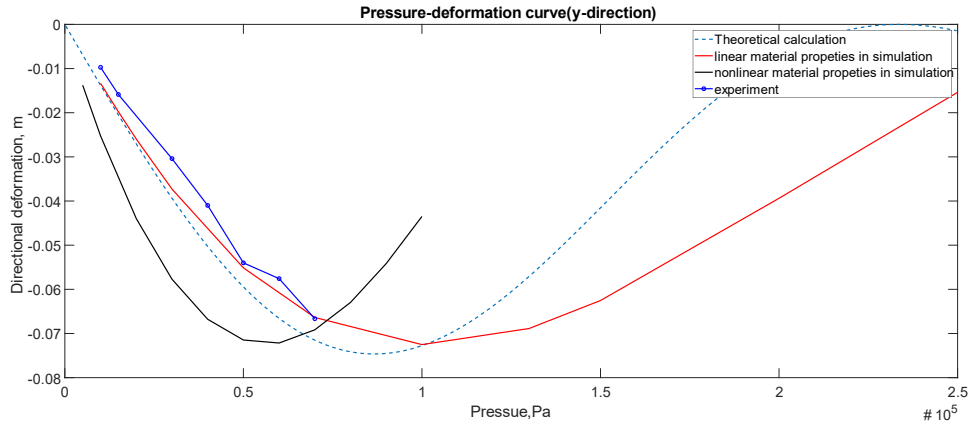


Figure 35 Comparison between experiment results, simulation, and theoretical in y-direction

Since the experimental results fit the curve of simulation results, to save time, the subsequent tests were simulated by ANSYS through the optimization module. There are two parameters which are considered as the parameters that can affect the deformation of the pneumatical bending actuator. These are the thickness of chamber walls and the walls over the air channel. The new model for simulation was also redesigned to achieve a more efficient computation time. The new model for simulation was four chambers instead of 14 as in the original. Based on previous comparison between experiment and simulation, the linear material properties simulation fits the experimental results more accurately. Moreover, the linear simulation is also close to the theoretical results. On account of the above reasons, the linear material properties simulation is selected as the base material. The new thickness of the chamber walls is optimized from 0.1 mm to 0.5 mm, and the range for the walls over the channel is from 0.4 mm to 1 mm. Each parameter is an independent variable in each single simulation while the other parameter is valued to the maximum value in the range interval.

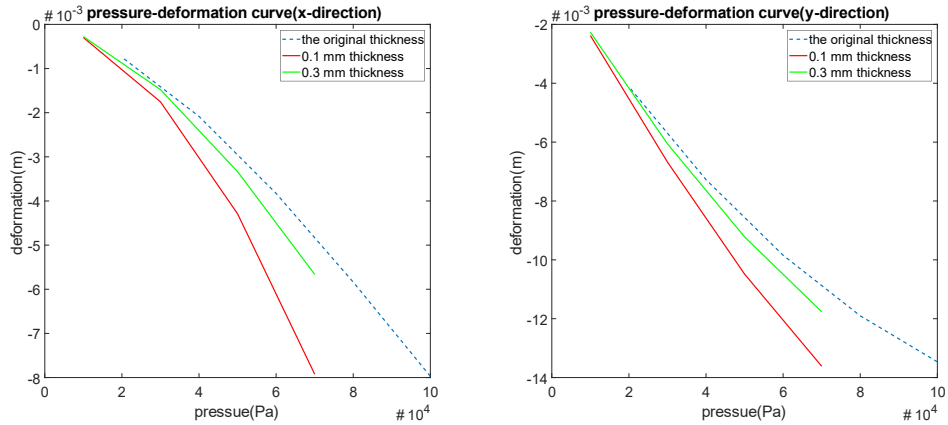


Figure 36 Comparison between different thickness of side walls

As shown in Figure 36, as the thickness of the chamber walls decreases, the deformation increases dramatically. Thicker walls mean that the shape change is larger than the undeformed design. The deformed two walls squeeze each other and push the upper half to elongate. Since the bottom is inextensible, the elongation of the upper half generates a bending moment for the actuator. Since the deformation of the two walls is not enough to touch each other under lower pressure the thickness of the wall has little effect for lower pressure, as shown is Figure 38(a). Under high pressure (Figure 38(b)), the mutual compression of the two walls creates additional bending moments. Therefore, the rate of deformation of the actuator will increase at larger pressure.

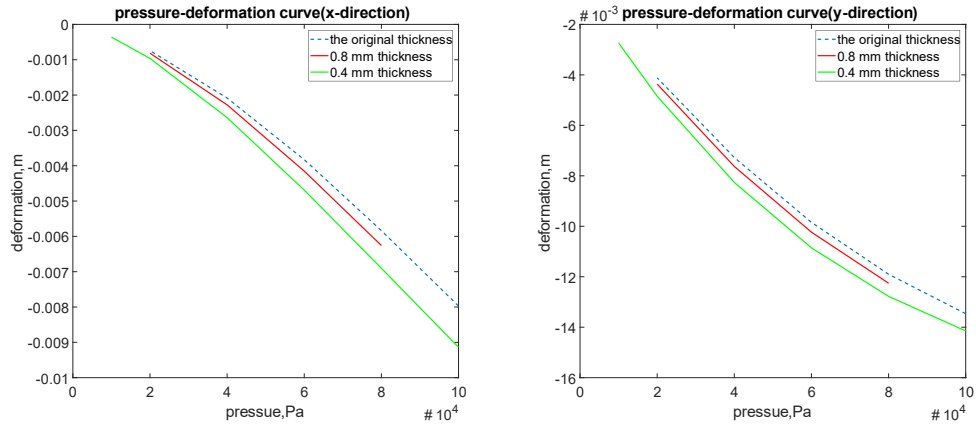


Figure 37 Comparison between different thickness of walls over channel

The simulation results for the control group of the thickness of the wall over air channel and the experimental group are shown as Figure 37. As can be seen from the figure, as the thickness decreases, the deformation at the same pressure increases. Although the slope of the pressure deformation curve is not a constant, the rate of change of the slope is substantially the same. This can also be derived from the fact that the three curves are essentially parallel.

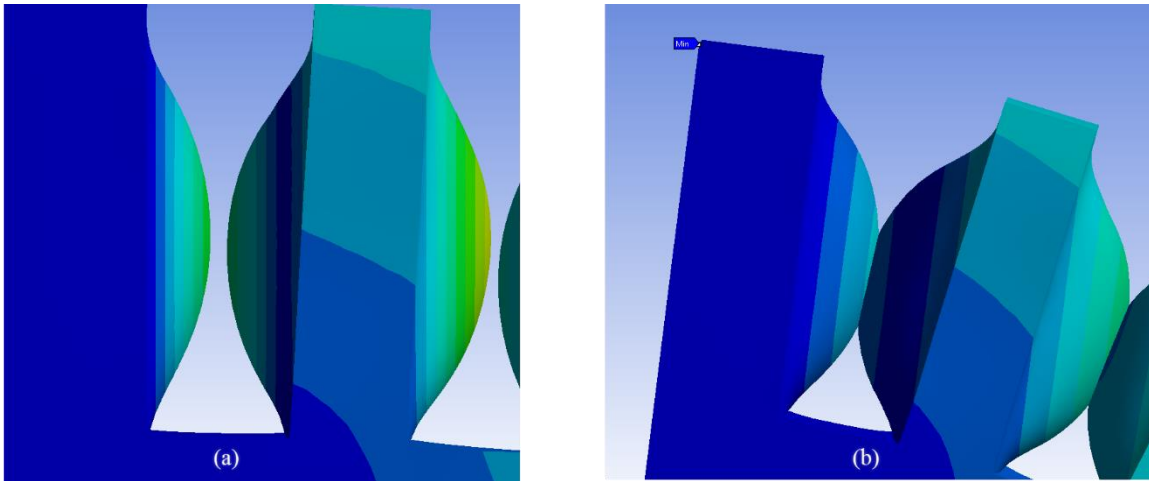


Figure 38 The touch situation at the same thickness of side walls in different pressure

CHAPTER 7

CONCLUSION

In this thesis, a simplified method for soft robotic actuator fabrication has been introduced. In mathematical forms, the pneumatic bending actuator can be considered as a cantilever with uniformly distributed load. The theoretical method provides a more intuitive way to observe and analyze the effect of each variable on the bending situation. This method applies an elastic approach instead of materials theory, so that it is more accurate for large deformation. This theory is helpful at evaluating the results of the simulation and experiments. For the Finite Element (FE) simulation, the pneumatic bending actuator has a fixed end in boundary condition and a free end. When pressurized, the actuator inflates, and the chambers are deflected. Based on the properties of material, the simulation was separated into two types, linear and nonlinear. The linear properties mean that the material has isotropic elasticity, which has a constant Young's Modulus. However, in reality, the properties of the NinjaFlex are nonlinear. Based on previous research, the hyperelastic model following a Yeoh 3rd order, was chosen. By comparing the linear, nonlinear, and experimental results, the nonlinear results, although somewhat erratic, are generally consistent with the theoretical and actual results curves.

In the subsequent study of wall thicknesses at two different locations in the pneumatic bending actuator, the simulation method was performed as a way to optimize the experimental method. From the experimental, the theoretical, and the linear, and nonlinear material simulation results, the simulation with linear material properties are considered a suitable way to optimize the 3D printed soft-robotic actuator design and fabrication. From the FE simulation, optimization of two variables was performed. With the thickness of the chamber walls as a variable, the rate of deformation suddenly increases after a certain internal pressure. After analysis, the conclusion

is that deformed walls under large pressure will squeeze each other and generate a bending moment. In the case where the thickness of the wall over the air channel is a parameter, the slope remains the same for the values in the optimization run. Under this set of simulations, the pressure-deformation curves of the control and experimental groups were almost parallel. The parallel phenomenon explained that the thickness of the wall over the air channel will only affect the size of the deformation but has little effect on the overall structure of the entire actuator.

REFERENCES

1. Webster III, R.J. and B.A. Jones, *Design and kinematic modeling of constant curvature continuum robots: A review*. The International Journal of Robotics Research, 2010. **29**(13): p. 1661-1683.
2. Trivedi, D., et al., *Soft robotics: Biological inspiration, state of the art, and future research*. Applied Bionics and Biomechanics, 2008. **5**(3): p. 99-117.
3. Odhner, L.U., et al., *A compliant, underactuated hand for robust manipulation*. The International Journal of Robotics Research, 2014. **33**(5): p. 736-752.
4. Wiener, N., *Cybernetics in history*. Theorizing in communication: Readings across traditions, 1954: p. 267-273.
5. Rus, D. and M.T. Tolley, *Design, fabrication and control of soft robots*. Nature, 2015. **521**(7553): p. 467.
6. Sangian, D., et al., *The effect of geometry and material properties on the performance of a small hydraulic McKibben muscle system*. Sensors and Actuators A: Physical, 2015. **234**: p. 150-157.
7. Sugisaka, M. and H. Zhao, *The characteristics of McKibben muscle based on the pneumatic experiment system*. Artificial Life and Robotics, 2007. **11**(2): p. 223-226.
8. Gonzales, A.V., et al. *TER: a system for robotic tele-echography*. in *International Conference on Medical Image Computing and Computer-Assisted Intervention*. 2001. Springer.
9. Chou, C.-P. and B. Hannaford, *Measurement and modeling of McKibben pneumatic artificial muscles*. IEEE Transactions on robotics and automation, 1996. **12**(1): p. 90-102.

10. Caldwell, D.G., G.A. Medrano-Cerda, and C.J. Bowler. *Investigation of bipedal robot locomotion using pneumatic muscle actuators*. in *Robotics and Automation, 1997. Proceedings., 1997 IEEE International Conference on*. 1997. IEEE.
11. Wisse, M. and J. Van Frankenhuyzen, *Design and construction of MIKE; a 2-D autonomous biped based on passive dynamic walking*, in *Adaptive motion of animals and machines*. 2006, Springer. p. 143-154.
12. Klute, G.K., J.M. Czerniecki, and B. Hannaford. *McKibben artificial muscles: pneumatic actuators with biomechanical intelligence*. in *Advanced Intelligent Mechatronics, 1999. Proceedings. 1999 IEEE/ASME International Conference on*. 1999. IEEE.
13. Daerden, F., *Conception and realization of pleated pneumatic artificial muscles and their use as compliant actuation elements*. Vrije Universiteit Brussel, Belgium, 1999.
14. Daerden, F. and D. Lefeber, *Pneumatic artificial muscles: actuators for robotics and automation*. *European journal of mechanical and environmental engineering*, 2002. **47**(1): p. 11-21.
15. Caldwell, D.G., G.A. Medrano-Cerda, and M. Goodwin, *Control of pneumatic muscle actuators*. *IEEE control systems*, 1995. **15**(1): p. 40-48.
16. Inoue, K. *Rubbertuators and applications for robots*. in *Proceedings of the 4th international symposium on Robotics Research*. 1988. MIT Press.
17. Caldwell, D.G., A. Razak, and M. Goodwin, *Braided pneumatic muscle actuators*. *IFAC Proceedings Volumes*, 1993. **26**(1): p. 522-527.
18. Holt, J.D., *Design and Testing of a Biomimetic Pneumatic Actuated Seahorse Tail Inspired Robot*. 2017.

19. Daerden, F. and D. Lefeber, *The concept and design of pleated pneumatic artificial muscles*. International Journal of Fluid Power, 2001. **2**(3): p. 41-50.
20. Wong, Z.Y., *Wearable power assisted pneumatic-based ankle foot orthosis*. 2012, UTAR.
21. Winters, J.M. *Braided artificial muscles: Mechanical properties and future uses in prosthetics/orthotics*. in *Proceedings of the RESNA 13th annual conference*. 1990. ERIC.
22. Beullens, T., *Hydraulic or pneumatic drive device*. 1989, Google Patents.
23. Driver, T. and X. Shen, *Sleeve muscle actuator: Concept and prototype demonstration*. Journal of Bionic Engineering, 2013. **10**(2): p. 222-230.
24. Yariott, J.M., *Fluid actuator*. 1972, Google Patents.
25. Immega, G. and M. Kukulj, *Axially contractable actuator*. 1990, Google Patents.
26. Bogunyà Piferrer, V., *The waterbomb actuator: a new origami-based pneumatic soft muscle*. 2016.
27. Suzumori, K., A. Koga, and H. Riyoko. *Microfabrication of integrated FMAs using stereo lithography*. in *Micro Electro Mechanical Systems, 1994, MEMS'94, Proceedings, IEEE Workshop on*. 1994. IEEE.
28. Hunter, I.W., J.M. Hollerbach, and J. Ballantyne, *A comparative analysis of actuator technologies for robotics*. Robotics Review, 1991. **2**: p. 299-342.
29. Ilievski, F., et al., *Soft robotics for chemists*. Angewandte Chemie, 2011. **123**(8): p. 1930-1935.
30. Kodama, H., *A scheme for three-dimensional display by automatic fabrication of three-dimensional model*. IEICE Trans. on Electronics, 1981: p. 237-241.

31. Kodama, H., *Automatic method for fabricating a three-dimensional plastic model with photo-hardening polymer*. Review of scientific instruments, 1981. **52**(11): p. 1770-1773.
32. Gabor, A., et al., *3D Printing of a Mandibular Bone Deffect*. MATERIALE PLASTICE, 2017. **54**(1): p. 29-31.
33. Wagner, J.B., et al., *Three professions come together for an interdisciplinary approach to 3D printing: occupational therapy, biomedical engineering, and medical librarianship*. Journal of the Medical Library Association: JMLA, 2018. **106**(3): p. 370.
34. Abdollahi, S., et al., *Expert-guided optimization for 3D printing of soft and liquid materials*. PloS one, 2018. **13**(4): p. e0194890.
35. Klein, G.T., Y. Lu, and M.Y. Wang, *3D printing and neurosurgery—ready for prime time?* World neurosurgery, 2013. **80**(3): p. 233-235.
36. Ventola, C.L., *Medical applications for 3D printing: current and projected uses*. Pharmacy and Therapeutics, 2014. **39**(10): p. 704.
37. Hoy, M.B., *3D printing: making things at the library*. Medical reference services quarterly, 2013. **32**(1): p. 93-99.
38. Mishra, M., *3D Printing Technology*. Science Horizon, 2014. **43**.
39. Bertrand, P., et al., *Ceramic components manufacturing by selective laser sintering*. Applied Surface Science, 2007. **254**(4): p. 989-992.
40. Rao, H., et al., *The influence of processing parameters on aluminium alloy A357 manufactured by Selective Laser Melting*. Materials & Design, 2016. **109**: p. 334-346.
41. Wang, P., et al., *Selective laser melting of Al-Zn-Mg-Cu: Heat treatment, microstructure and mechanical properties*. Journal of Alloys and Compounds, 2017. **707**: p. 287-290.

42. Danezan, A., et al., *Selective laser sintering of porcelain*. Journal of the European Ceramic Society, 2018. **38**(2): p. 769-775.
43. Olakanmi, E.O.t., R. Cochrane, and K. Dalgarno, *A review on selective laser sintering/melting (SLS/SLM) of aluminium alloy powders: Processing, microstructure, and properties*. Progress in Materials Science, 2015. **74**: p. 401-477.
44. Ngo, T.D., et al., *Additive manufacturing (3D printing): A review of materials, methods, applications and challenges*. Composites Part B: Engineering, 2018.
45. Mohamed, O.A., S.H. Masood, and J.L. Bhowmik, *Optimization of fused deposition modeling process parameters: a review of current research and future prospects*. Advances in Manufacturing, 2015. **3**(1): p. 42-53.
46. Sood, A.K., R.K. Ohdar, and S.S. Mahapatra, *Parametric appraisal of mechanical property of fused deposition modeling processed parts*. Materials & Design, 2010. **31**(1): p. 287-295.
47. Chohan, J.S., et al., *Dimensional accuracy analysis of coupled fused deposition modeling and vapour smoothing operations for biomedical applications*. Composites Part B: Engineering, 2017. **117**: p. 138-149.
48. Parandoush, P. and D. Lin, *A review on additive manufacturing of polymer-fiber composites*. Composite Structures, 2017. **182**: p. 36-53.
49. Wang, X., et al., *3D printing of polymer matrix composites: A review and prospective*. Composites Part B: Engineering, 2017. **110**: p. 442-458.
50. Bae, E.-J., et al., *A comparative study of additive and subtractive manufacturing for dental restorations*. The Journal of prosthetic dentistry, 2017. **118**(2): p. 187-193.

51. Song, S.Y., et al., *Improvement of dispersion stability and 3D-printing characteristics of ceramics in photopolymers by controlling the coating thickness of silane coupling agents*. Materials Chemistry and Physics, 2018.
52. Martinez, P.R., et al., *Influence of Geometry on the Drug Release Profiles of Stereolithographic (SLA) 3D-Printed Tablets*. AAPS PharmSciTech: p. 1-7.
53. Campana, G. and M. Mele, *An application to Stereolithography of a feature recognition algorithm for manufacturability evaluation*. Journal of Intelligent Manufacturing, 2018: p. 1-16.
54. Bhavar, V., et al. *A review on powder bed fusion technology of metal additive manufacturing*. in *4th International Conference and Exhibition on Additive Manufacturing Technologies-AM-2014, September*. 2014.
55. Ventola, L., et al., *Rough surfaces with enhanced heat transfer for electronics cooling by direct metal laser sintering*. International Journal of Heat and Mass Transfer, 2014. **75**: p. 58-74.
56. Gratton, A., *Comparison of mechanical, metallurgical properties of 17-4PH stainless steel between direct metal laser sintering (DMLS) and traditional manufacturing methods*. 2012 NCUR, 2012.
57. Calignano, F., et al., *Influence of process parameters on surface roughness of aluminum parts produced by DMLS*. The International Journal of Advanced Manufacturing Technology, 2013. **67**(9-12): p. 2743-2751.
58. Manfredi, D., et al., *From powders to dense metal parts: Characterization of a commercial AlSiMg alloy processed through direct metal laser sintering*. Materials, 2013. **6**(3): p. 856-869.

59. Shellabear, M. and O. Nyrhilä, *DMLS-Development history and state of the art*. Laser Assisted Netshape Engineering 4, Proceedings of the 4th LANE, 2004: p. 21-24.
60. Bendsøe, M.P. and N. Kikuchi, *Generating optimal topologies in structural design using a homogenization method*. Computer methods in applied mechanics and engineering, 1988. **71**(2): p. 197-224.
61. Bendsøe, M.P., *Optimal shape design as a material distribution problem*. Structural optimization, 1989. **1**(4): p. 193-202.
62. Xie, Y.M. and G.P. Steven, *A simple evolutionary procedure for structural optimization*. Computers & structures, 1993. **49**(5): p. 885-896.
63. Allaire, G., F. Jouve, and A.-M. Toader, *A level-set method for shape optimization*. Comptes Rendus Mathematique, 2002. **334**(12): p. 1125-1130.
64. Huang, X. and Y. Xie, *Bi-directional evolutionary topology optimization of continuum structures with one or multiple materials*. Computational Mechanics, 2009. **43**(3): p. 393.
65. de Payrebrune, K.M. and O.M. O'Reilly, *On constitutive relations for a rod-based model of a pneu-net bending actuator*. Extreme Mechanics Letters, 2016. **8**: p. 38-46.
66. Scott, W.L. and D.A. Paley. *Geometric gait design for a starfish-inspired robot with curvature-controlled soft actuators*. in *ASME 2017 Dynamic Systems and Control Conference*. 2017. American Society of Mechanical Engineers.
67. Wang, X., L. Yunshuai, and Y. Feng, *Analytical Solution of the Elastic Mechanics for Cantilever Beam under the Even Loads*. Journal of Gansu Sciences, 2013. **25**(3).
68. Madden, J.D., *Mobile robots: motor challenges and materials solutions*. science, 2007. **318**(5853): p. 1094-1097.

69. Polygerinos, P., et al. *Towards a soft pneumatic glove for hand rehabilitation*. in *Intelligent Robots and Systems (IROS), 2013 IEEE/RSJ International Conference on*. 2013. IEEE.
70. Shepherd, R.F., et al., *Multigait soft robot*. *Proceedings of the national academy of sciences*, 2011. **108**(51): p. 20400-20403.
71. Mosadegh, B., et al., *Pneumatic networks for soft robotics that actuate rapidly*. *Advanced functional materials*, 2014. **24**(15): p. 2163-2170.
72. NinjaTek, *technical specifications*.
73. HOBERT, E., *3D Printed Flexible Fingertip Strain Sensor*. 2017, UNIVERSITY OF TWENTE.
74. ANSYS, *engineering data source*. 2018.
75. Rivlin, R., *Large elastic deformations of isotropic materials IV. Further developments of the general theory*. *Phil. Trans. R. Soc. Lond. A*, 1948. **241**(835): p. 379-397.
76. Boulanger, P. and M. Hayes, *Finite-amplitude waves in Mooney-Rivlin and Hadamard materials*, in *Topics in finite elasticity*. 2001, Springer. p. 131-167.
77. Macosko, C.W. and R.G. Larson, *Rheology: principles, measurements, and applications*. 1994.
78. Yeoh, O.H., *Some forms of the strain energy function for rubber*. *Rubber Chemistry and technology*, 1993. **66**(5): p. 754-771.
79. Rivlin, R., *Some applications of elasticity theory to rubber engineering*, in *Collected papers of RS Rivlin*. 1997, Springer. p. 9-16.
80. Yap, H.K., H.Y. Ng, and C.-H. Yeow, *High-force soft printable pneumatics for soft robotic applications*. *Soft Robotics*, 2016. **3**(3): p. 144-158.

APPENDIX A

The Office of Research Integrity Approval Letter



Office of Research Integrity

November 20, 2018

Chenyu Zheng
1616 Spring Valley Dr., Apt 37
Huntington, WV 25704

Dear Chenyu:

This letter is in response to the submitted thesis abstract entitled "*Design and Simulation of a Pneumatic Actuator Bending Soft Robotics Based on 3D Printing.*" After assessing the abstract, it has been deemed not to be human subject research and therefore exempt from oversight of the Marshall University Institutional Review Board (IRB). The Code of Federal Regulations (45CFR46) has set forth the criteria utilized in making this determination. Since the information in this study does not involve human subjects as defined in the above referenced instruction, it is not considered human subject research. If there are any changes to the abstract you provided then you would need to resubmit that information to the Office of Research Integrity for review and a determination.

I appreciate your willingness to submit the abstract for determination. Please feel free to contact the Office of Research Integrity if you have any questions regarding future protocols that may require IRB review.

Sincerely,

A handwritten signature in blue ink that reads 'Bruce F. Day'.

Bruce F. Day, ThD, CIP
Director

WE ARE... MARSHALL.

One John Marshall Drive • Huntington, West Virginia 25755 • Tel 304/696-4303
A State University of West Virginia • An Affirmative Action/Equal Opportunity Employer

APPENDIX B

Data from Simulations and Experiment

Table 5 Data collected from linear material simulation in ANSYS

Name	pressure	$D_{x_{max}}$	$D_{x_{min}}$	$D_{y_{max}}$	$D_{y_{min}}$	$D_{x_{average}}$	$D_{y_{average}}$
unit	Pa	m	m	m	m	m	m
	10000	-0.00113	-0.00115	-0.01329	-0.0134	-0.00114	-0.01334
	15000	-0.00253	-0.00258	-0.0197	-0.01986	-0.00256	-0.01978
	20000	-0.00446	-0.00454	-0.02585	-0.02606	-0.0045	-0.02596
	30000	-0.00965	-0.00979	-0.03715	-0.03743	-0.00972	-0.03729
	50000	-0.02384	-0.02413	-0.05497	-0.0553	-0.02398	-0.05513
	70000	-0.04055	-0.04098	-0.06622	-0.06652	-0.04076	-0.06637
	100000	-0.06626	-0.0668	-0.07241	-0.07262	-0.06653	-0.07251
	130000	-0.08822	-0.08871	-0.06878	-0.06897	-0.08847	-0.06887
	150000	-0.10011	-0.10062	-0.06241	-0.06266	-0.10037	-0.06253
	200000	-0.11629	-0.11673	-0.03922	-0.03954	-0.11651	-0.03938
	250000	-0.11007	-0.11007	-0.01513	-0.01563	-0.11007	-0.01538

Table 6 Data collected from nonlinear material simulation in ANSYS

Name	pressure	$D_{x_{max}}$	$D_{x_{min}}$	$D_{y_{max}}$	$D_{y_{min}}$	$D_{x_{average}}$	$D_{y_{average}}$
unit	Pa	m	m	m	m	m	m
	5000	-0.00141	-0.00142	-0.01377	-0.01377	-0.00142	-0.01377
	10000	-0.00463	-0.00465	-0.02524	-0.02526	-0.00464	-0.02525
	20000	-0.01477	-0.01477	-0.04396	-0.04396	-0.01477	-0.04396
	30000	-0.02819	-0.02819	-0.0577	-0.0577	-0.02819	-0.0577
	40000	-0.04339	-0.04339	-0.06678	-0.06678	-0.04339	-0.06678
	50000	-0.05917	-0.05925	-0.07147	-0.07147	-0.05921	-0.07147
	60000	-0.07465	-0.07476	-0.07216	-0.07216	-0.07471	-0.07216
	70000	-0.08913	-0.08924	-0.06915	-0.06919	-0.08918	-0.06917
	80000	-0.10174	-0.10174	-0.06296	-0.06296	-0.10174	-0.06296
	90000	-0.11187	-0.11187	-0.05411	-0.05421	-0.11187	-0.05416
	100000	-0.11885	-0.11885	-0.04344	-0.04355	-0.11885	-0.04349

Table 7 Data collected from experiments

Name	Pressure	D_x	D_y	$D_{x\text{average}}$	$D_{y\text{average}}$
unit	Pa	mm	mm	mm	mm
		-1	-7.5		
		-1.5	-9		
	10000	-1	-10	-1.42857	-9.71429
		-2.5	-14		
		-1.5	-9.5		
		-1.5	-9		
		-1	-9		
		-1.5	-15		
	15000	-1.5	-15	-1.625	-15.875
		-1.5	-15.5		
		-2	-18		
		-7	-29.5		
		-7	-29.5		
	30000	-8.5	-31	-7.9	-30.4
		-8.5	-31		
		-8.5	-31		
		-11.5	-39.5		
		-11.5	-39.5		
	40000	-12.5	-41.5	-12.3	-41
		-12.5	-41.5		
		-13.5	-43		
		-16	-50		
		-18	-52		
		-18	-52		
	50000	-20	-52.5	-21.7857	-54
		-25.5	-55		
		-27	-57		
		-28	-59.5		
		-26	-55		
		-29	-57		
		-30	-58		
	60000	-31.5	-59	-29.7143	-57.5714
		-29	-57		
		-30	-58		
		-32.5	-59		
		-39.5	-65		
		-40.5	-65.5		
		-42.5	-66		
	70000	-45	-67.5	-43	-66.6429
		-46	-69		
		-42.5	-66		
		-45	-67.5		

Table 8 Data collected from different thickness of side walls in ANSYS

Name	pressure	$D_{x_{min}}$	$D_{x_{max}}$	$D_{x_{average}}$	$D_{y_{min}}$	$D_{y_{max}}$	$D_{y_{average}}$
unit	Pa	m	m	m	m	m	m
Thickness = 0.1 mm							
	70000	-0.00797	-0.00787	-0.00792	-0.01366	-0.01357	-0.01362
	50000	-0.00431	-0.00427	-0.00429	-0.01054	-0.01043	-0.01048
	30000	-0.00176	-0.00175	-0.00175	-0.00672	-0.00664	-0.00668
	10000	-0.00031	-0.00029	-0.0003	-0.0024	-0.00236	-0.00238
Thickness = 0.3 mm							
	70000	-0.00569	-0.00564	-0.00566	-0.01182	-0.01171	-0.01176
	50000	-0.00335	-0.00333	-0.00334	-0.00927	-0.00917	-0.00922
	30000	-0.00149	-0.00147	-0.00148	-0.0061	-0.00601	-0.00606
	10000	-0.00029	-0.00026	-0.00028	-0.00229	-0.00224	-0.00226

Table 9 Data collected from different thickness of the wall over the channel in ANSYS

Name	pressure	$D_{x_{min}}$	$D_{x_{max}}$	$D_{x_{average}}$	$D_{y_{min}}$	$D_{y_{max}}$	$D_{y_{average}}$
unit	Pa	m	m	m	m	m	m
Thickness = 0.8 mm							
	80000	-0.00629	-0.00623	-0.00626	-0.01232	-0.01219	-0.01226
	60000	-0.00417	-0.00414	-0.00415	-0.0103	-0.01017	-0.01023
	40000	-0.00229	-0.00227	-0.00228	-0.00758	-0.00768	-0.00763
	20000	-0.00083	-0.0008	-0.00082	-0.0044	-0.00433	-0.00437
Thickness = 0.4 mm							
	100000	-0.00918	-0.0091	-0.00914	-0.0142	-0.0141	-0.01415
	80000	-0.00693	-0.00688	-0.0069	-0.01283	-0.01273	-0.01278
	60000	-0.00471	-0.00468	-0.00469	-0.0109	-0.01081	-0.01086
	40000	-0.00265	-0.00263	-0.00264	-0.00831	-0.00822	-0.00826
	20000	-0.00097	-0.00095	-0.00096	-0.00488	-0.00481	-0.00485
	10000	-0.00037	-0.00035	-0.00036	-0.00276	-0.00271	-0.00273

APPENDIX C

Matlab code

Displacement_linear_simulation_vs_theoretical.m

```
function displacement_linear_simulation_vs_theoretical
clc
%%
w=0.017
c=0.003
H=0.012
E = 12000000
Poir = 0.48
L = 0.103
t=0.002
h=(H+t)/2
y=-h
l=L/2
x=1
%%
for i = 1:1000                                %To get theoretical displacement data
from 0 Pa to 250,000 Pa .
        P(i) =250*(i-1)

K_new(i) =K_new(P(i))                        %Using pressure to calculate curve.
s=0.103                                       %This is the length of bending actuator.
                                             %If K is not equal to 0, calculate
curve at end of actuator( s= 0.103 m).
        disx(i) = (1./K_new(i)).*(sin(K_new(i).*s))-0.103 ;
        disy(i) = -(1./K_new(i)).*(1-cos(K_new(i).*s));
end
%%
p_linear=[10000,15000,20000,30000,50000,70000,100000,130000,150000,200000,250
000];
x_linear=[-0.00113715,-0.0025584,-0.00449795,-0.00972005,-0.023984,-
0.0407625,-0.06653,-0.088466,-0.100365,-0.11651,-0.11007];
y_linear=[-0.0133435;-0.0197805;-0.0259565;-0.0372905;-0.0551305;-0.0663675;-
0.072514;-0.068873;-0.0625325;-0.039379;-0.0153785];
%%
figure
plot(P,disx,'-', 'linewidth',2)
hold on
plot(p_linear,x_linear,'r', 'linewidth',2)
hold on
legend('Theoretical calculation','linear material propeties in simulation')
title('pressure-deformation curve(x-direction)')
xlabel('pressue,Pa')
ylabel('deformation,m')
set(gca,...
'FontSize',24)
%%
figure
```

```

plot(P,disy,'-', 'linewidth',2)
hold on
plot(p_linear,y_linear,'r', 'linewidth',2)
hold on
legend('Theoretical calculation', 'linear material propeties in simulation')
title('pressure-deformation curve(y-direction)')
xlabel('pressue,Pa')
ylabel('deformation,m')
set(gca,...
'FontSize',24)
hold on
end
%%
function K_new = K_new(P)
w=0.017
c=0.003
H=0.012
E = 1200000
Poir = 0.48
L = 0.103
t=0.002
h=0.002
l=L/2
x=1
q = P*H^2*c*w/(L^3)
K_new = (1/E)*((3*Poir*q)/(4*h^3)+(3*q*(x^2+2*1*x+1^2)/(4*h^3))-
(3*q*(8+5*Poir)/(5*h)))
end

```

Displacement_nonlinear_simulation_vs_theoretical.m

```

function displacement_nonlinear_simulation_vs_theoretical
clc
%%
w=0.017
c=0.003
H=0.012
E = 12000000
Poir = 0.48
L = 0.103
t=0.002
h=(H+t)/2
y=-h
l=L/2
x=1
%%
for i = 1:1000 %To get theoretical displacement data
from 0 Pa to 250,000 Pa .
P(i) =250*(i-1)

K_new(i) =K_new(P(i)) %Using pressure to calculate curve.
s=0.103 %This is the length of bending actuator.
%If K is not equal to 0, calculate
curve at end of actuator( s= 0.103 m).
disx(i) = (1./K_new(i)).*(sin(K_new(i).*s))-0.103 ;

```

```

        disy(i) = -(1./K_new(i)).*(1-cos(K_new(i).*s));
end
%%
p_nonlinear
=[5000,10000,20000,30000,40000,50000,60000,70000,80000,90000,100000];
x_nonlinear =[-0.001417,-0.00464025,-0.014771,-0.028188,-0.043392,-0.059212,-
0.0747055,-0.0891805,-0.10174,-0.11187,-0.11885];
y_nonlinear =[-0.013772;-0.02525;-0.043963;-0.057701;-0.066775;-0.071473;-
0.072155;-0.069168;-0.062961;-0.054158;-0.043494];
%%
figure
plot(P,disx,'-', 'linewidth',2)
hold on
plot(p_nonlinear,x_nonlinear,'r', 'linewidth',2)
hold on
legend('Theoretical calculation','nonlinear material propeties in simulation')
title('pressure-deformation curve(x-direction)')
xlabel('pressue,Pa')
ylabel('deformation,m')
set(gca,...
'FontSize',24)
%%
figure
plot(P,disy,'-', 'linewidth',2)
hold on
plot(p_nonlinear,y_nonlinear,'r', 'linewidth',2)
hold on
legend('Theoretical calculation','nonlinear material propeties in simulation')
title('pressure-deformation curve(y-direction)')
xlabel('pressue,Pa')
ylabel('deformation,m')
set(gca,...
'FontSize',24)
hold on
end
%%
function K_new = K_new(P)
w=0.017
c=0.003
H=0.012
E = 1200000
Poir = 0.48
L = 0.103
t=0.002
h=0.002
l=L/2
x=1
q = P*H^2*c*w/(L^3)
K_new = (1/E)*((3*Poir*q)/(4*h^3)+(3*q*(x^2+2*1*x+1^2)/(4*h^3))-
(3*q*(8+5*Poir)/(5*h)))
End

```

Displacement_exp.m

```

function displacement_exp
clc
%%

```

```

w=0.017
c=0.003
H=0.013
E = 12000000
Poir = 0.48
L = 0.103
t=0.002
h=(H+t)/2
y=-h
l=L/2
x=1
%%
for i = 1:1000                                %To get theoretical displacement data
from 0 Pa to 250,000 Pa .
        P(i) =250*(i-1)

K_new(i) =K_new(P(i))                        %Using pressure to calculate curve.
s=0.103                                       %This is the length of bending actuator.
                                                %If K is not equal to 0, calculate
curve at end of actuator( s= 0.103 m).
        disx(i) = (1./K_new(i)).*(sin(K_new(i).*s))-0.103 ;
        disy(i) = -(1./K_new(i)).*(1-cos(K_new(i).*s));
end
%%
p_linear=[10000,15000,20000,30000,50000,70000,100000,130000,150000,200000,250
000];
x_linear=[-0.00113715,-0.0025584,-0.00449795,-0.00972005,-0.023984,-
0.0407625,-0.06653,-0.088466,-0.100365,-0.11651,-0.11007];
y_linear=[-0.0133435;-0.0197805;-0.0259565;-0.0372905;-0.0551305;-0.0663675;-
0.072514;-0.068873;-0.0625325;-0.039379;-0.0153785];
%%
p_nonlinear
=[5000,10000,20000,30000,40000,50000,60000,70000,80000,90000,100000];
x_nonlinear =[-0.001417,-0.00464025,-0.014771,-0.028188,-0.043392,-0.059212,-
0.0747055,-0.0891805,-0.10174,-0.11187,-0.11885];
y_nonlinear      =[-0.013772;-0.02525;-0.043963;-0.057701;-0.066775;-0.071473;-
0.072155;-0.069168;-0.062961;-0.054158;-0.043494];
%%
p_exp=[10000,15000,30000,40000,50000,60000,70000]
x_exp=0.001*[-1.42857,-1.625,-7.9,-12.3,-21.7857,-29.7143,-43]
y_exp=0.001*[-9.714285714;-15.875;-30.4;-41;-54;-57.57142857;-66.64285714]
%%
figure
plot(P,disx,'--','linewidth',2)
hold on
plot(p_linear,x_linear,'r','linewidth',2)
hold on
plot(p_nonlinear,x_nonlinear,'black','linewidth',2)
hold on
plot(p_exp,x_exp,'blue-o','linewidth',2)

legend('Theoretical calculation','linear material propeties in
simulation','nonlinear material propeties in simulation','experiment')
title('Pressure-deformation curve(x-direction)')
xlabel('Pressue,Pa')
ylabel('Directional deformation, m')

```

```

set(gca,...
'FontSize',24)
%%
figure
plot(P,disy,'--','linewidth',2)
hold on
plot(p_linear,y_linear,'r','linewidth',2)
hold on
plot(p_nonlinear,y_nonlinear,'black','linewidth',2)
hold on
plot(p_exp,y_exp,'blue-o','linewidth',2)

legend('Theoretical calculation','linear material propeties in
simulation','nonlinear material propeties in simulation','experiment')
title('Pressure-deformation curve(y-direction)')
xlabel('Pressue,Pa')
ylabel('Directional deformation, m')
set(gca,...
'FontSize',24)
hold on
end
%%
function K_new = K_new(P)
w=0.017
c=0.003
H=0.013
E = 1200000
Poir = 0.48
L = 0.103
t=0.002
h=0.002
l=L/2
x=1
q = P*H^2*c*w/(L^3)
K_new = (1/E)*((3*Poir*q)/(4*h^3)+(3*q*(x^2+2*1*x+1^2)/(4*h^3))-
(3*q*(8+5*Poir)/(5*h)))
end

```

Displacement_linear_nonlinear.m

```

function displacement_linear_nonlinear
clc
%%
w=0.017
c=0.003
H=0.012
E = 12000000
Poir = 0.48
L = 0.103
t=0.002
h=(H+t)/2
y=-h
l=L/2
x=1
%%
for i = 1:1000 %To get theoretical displacement data
from 0 Pa to 250,000 Pa .

```

```

        P(i) =250*(i-1)

K_new(i) =K_new(P(i))           %Using pressure to calculate curve.
s=0.103                          %This is the length of bending actuator.
                                %If K is not equal to 0, calculate
curve at end of actuator( s= 0.103 m).
        disx(i) = (1./K_new(i)).*(sin(K_new(i).*s))-0.103 ;
        disy(i) = -(1./K_new(i)).*(1-cos(K_new(i).*s));

end
%%
p_linear=[10000,15000,20000,30000,50000,70000,100000,130000,150000,200000,250
000];
x_linear=[-0.00113715,-0.0025584,-0.00449795,-0.00972005,-0.023984,-
0.0407625,-0.06653,-0.088466,-0.100365,-0.11651,-0.11007];
y_linear=[-0.0133435;-0.0197805;-0.0259565;-0.0372905;-0.0551305;-0.0663675;-
0.072514;-0.068873;-0.0625325;-0.039379;-0.0153785];
%%
p_nonlinear
=[5000,10000,20000,30000,40000,50000,60000,70000,80000,90000,100000];
x_nonlinear =[-0.001417,-0.00464025,-0.014771,-0.028188,-0.043392,-0.059212,-
0.0747055,-0.0891805,-0.10174,-0.11187,-0.11885];
y_nonlinear      =[-0.013772;-0.02525;-0.043963;-0.057701;-0.066775;-0.071473;-
0.072155;-0.069168;-0.062961;-0.054158;-0.043494];

%%
figure
plot(P,disx,'--','linewidth',2)
hold on
plot(p_linear,x_linear,'r','linewidth',2)
hold on
plot(p_nonlinear,x_nonlinear,'black','linewidth',2)
hold on
legend('Theoretical calculation','linear material propeties in
simulation','nonlinear material propeties in simulation')
title('pressure-deformation curve(x-direction)')
xlabel('pressue,Pa')
ylabel('deformation,m')
set(gca,...
'FontSize',24)
%%
figure
plot(P,disy,'--','linewidth',2)
hold on
plot(p_linear,y_linear,'r','linewidth',2)
hold on
plot(p_nonlinear,y_nonlinear,'black','linewidth',2)
hold on
legend('Theoretical calculation','linear material propeties in
simulation','nonlinear material propeties in simulation')
title('pressure-deformation curve(y-direction)')
xlabel('pressue,Pa')
ylabel('deformation,m')
set(gca,...
'FontSize',24)
hold on
end

```

```

%%
function K_new = K_new(P)
w=0.017
c=0.003
H=0.012
E = 1200000
Poir = 0.48
L = 0.103
t=0.002
h=0.002
l=L/2
x=1
q = P*H^2*c*w/(L^3)
K_new = (1/E)*((3*Poir*q)/(4*h^3)+(3*q*(x^2+2*l*x+l^2)/(4*h^3))-
(3*q*(8+5*Poir)/(5*h)))
end

```

hyperelastic_curve.m

```

function hyperelastic_curve
%%
%this code is for generate figures of three types of hyperelastic model
%x is the value of strain
%y is the value of stress
%%
%Neo-Hookean model
Neo_x
=[0.134,0.268,0.357,0.624,0.892,1.16,1.43,2.05,2.59,3.03,3.79,4.37,4.82,5.17,
5.44,5.71,5.93,6.06,6.2,6.33,6.47,6.55,6.64]
Neo_y=[142032.056,288890.444,386796.036,670860.148,944582.12,1199688.24,14547
94.36,2027059.44,2509692.64,2902693.96,3564590.92,4067908.4,4454014.96,476427
9.16,4998701,5226228.08,5419281.36,5536492.28,5653703.2,5770914.12,5881230.28
,5957072.64,6039809.76]
%%
%Mooney-Rivlin model
Mooney_x =
[0.1338,0.2675,0.3567,0.6242,0.8917,1.1592,1.4268,2.051,2.586,3.0318,3.7898,4
.3694,4.8153,5.172,5.4395,5.707,5.9299,6.0637,6.1975,6.3312,6.465,6.5541,6.64
33];
Mooney_y =
[494.1474492,912.7972764,1172.453938,1941.495468,2803.754154,3869.063522,5245
.395513,10378.82012,18192.58268,28438.67868,57755.1982,94951.87682,135751.619
1,178064.7612,216504.4272,261538.9311,304701.5076,333300.2826,364061.2544,397
079.5705,432533.1159,457543.8578,483751.5301]
%%
%Yeoh model
Yeoh_x =
[0,0.011665,0.022715,0.033918,0.045122,0.055711,0.066454,0.077351,0.088094,0.
09899,0.109581,0.120323,0.131067,0.141503,0.1524,0.162836,0.173732,0.184015,0.
194758,0.205194,0.215477,0.225913,0.236656,0.247553,0.25845,0.268733,0.27978
3,0.290372,0.300808,0.311552,0.322294,0.333038,0.343781,0.354831,0.365267,0.3
76317,0.386447,0.39673,0.407625,0.418062,0.428958,0.439548,0.449985,0.460267,
0.471317,0.4816,0.492343,0.502933,0.51383,0.523959,0.534702,0.544984,0.555574

```

```

,0.56601,0.576446,0.587036,0.597319,0.607448,0.617577,0.628013,0.638143,0.648
272,0.658401,0.66853,0.67866]
Yeoh_y=[0,85112,140359,188141,227960,264045,299633,329993,359360,388228,41411
0,439494,463882,487276,508678,529831,550736,570895,590305,610214,628381,64654
9,664467,683132,700552,717724,734895,753560,769488,786410,801591,819509,83518
8,852110,868287,884960,900888,917810,933738,949914,967085,983013,1000433,1017
853,1034279,1051450,1070115,1088531,1107195,1127851,1146267,1166674,1187080,1
209728,1231379,1255269,1280156,1305541,1332915,1361784,1392891,1424994,146083
1,1499653,1541960]
%%
%generating figure
figure
subplot(131)
plot(Neo_x,Neo_y,'black-o')
legend('Neo-Hookean model')
hold on
title('Neo-Hookean model')
xlabel('Strain')
ylabel('Stress, Pa')
set(gca,...
'FontSize',24)
subplot(132)
plot(Mooney_x,Mooney_y,'black-o')
legend('Mooney-Rivlin model')
hold on
title('Mooney-Rivlin model')
xlabel('Strain')
ylabel('Stress, Pa')
set(gca,...
'FontSize',24)
subplot(133)
plot(Yeoh_x,Yeoh_y,'black-o')
legend('Yeoh model')
hold on

title('Yeoh model')
xlabel('Strain')
ylabel('Stress, Pa')
set(gca,...
'FontSize',24)
End

```

Curve1.m

```

function curve1
%%
%this code is for comparing the original displacement-pressure curve and
%the displacement-pressure with different thicknesses of side wall.
%%
%Original displacement-pressure curve data
original_p=[
100000
80000
60000
40000

```

```

20000]

original_x=[
-0.00797205
-0.0058371
-0.0038286
-0.00208335
-0.000742395]

original_y=[
-0.0134655
-0.011901
-0.00984455
-0.00727595
-0.0041185]
%%
%the displacement-pressure data when side walls thickness is equal to 0.1mm.
t_01_p =[70000
50000
30000
10000]
t_01_x=[-0.00792295
-0.00429145
-0.0017536
-0.000297595]
t_01_y=[-0.0136155
-0.010484
-0.00667785
-0.0023764]
%%
%the displacement-pressure data when side walls thickness is equal to 0.3mm.
t_03_p=[70000
50000
30000
10000]

t_03_x=[-0.00566325
-0.0033357
-0.00147695
-0.000276005]

t_03_y=[-0.011764
-0.00922065
-0.00605755
-0.00226475]

%%
subplot(1,2,1)
plot(original_p,original_x,'--','linewidth',2)
hold on
plot(t_01_p,t_01_x,'r','linewidth',2)
hold on
plot(t_01_p,t_03_x,'green','linewidth',2)
title('pressure-deformation curve(x-direction)')
xlabel('pressue (Pa) ')
ylabel('deformation(m) ')

```

```

legend('the original thickness','0.1 mm thickness','0.3 mm thickness')
set(gca,...
'FontSize',24)
subplot(1,2,2)
plot(original_p,original_y,'--','linewidth',2)
hold on
plot(t_01_p,t_01_y,'r','linewidth',2)
hold on
plot(t_01_p,t_03_y,'green','linewidth',2)
title('pressure-deformation curve(y-direction)')
xlabel('pressue (Pa)')
ylabel('deformation(m)')
legend('the original thickness','0.1 mm thickness','0.3 mm thickness')
set(gca,...
'FontSize',24)
end

```

Curve2.m

```

function curve2
%%
%this code is for comparing the original displacement-pressure curve and
%the displacement-pressure with different thicknesses of the wall over the
channel.
%%
%Original displacement-pressure curve data
original_p=[100000;80000;60000;40000;20000]
original_x=[-0.00797205;-0.0058371;-0.0038286;-0.00208335;-0.000742395]
original_y=[-0.0134655;-0.011901;-0.00984455;-0.00727595;-0.0041185]
%%
%the displacement-pressure data when the thickness of the wall over the channel
is equal to 0.8mm.
top_p_08 =[80000;60000;40000;20000]
top_x_08 =[-0.0062586;-0.0041531;-0.0022771;-0.00081507]
top_y_08 =[-0.012255;-0.010233;-0.00762955;-0.004365]
%%
%the displacement-pressure data when the thickness of the wall over the channel
is equal to 0.4mm.
top_p_04 =[100000;80000;60000;40000;20000;10000]
top_x_04 =[-0.00914005;-0.00690285;-0.0046917;-0.00263865;-0.00096231;-
0.000359215]
top_y_04 =[-0.0141485;-0.012777;-0.010855;-0.00826265;-0.0048473;-0.002733]

subplot(1,2,1)
plot(original_p,original_x,'--','linewidth',2)
hold on
plot(top_p_08,top_x_08,'r','linewidth',2)
hold on
plot(top_p_04,top_x_04,'green','linewidth',2)
title('pressure-deformation curve(x-direction)')
xlabel('pressue, Pa')
ylabel('deformation,m')

```

```

legend('the original thickness','0.8 mm thickness','0.4 mm thickness')
set(gca,...
'FontSize',24)
subplot(1,2,2)
plot(original_p,original_y,'--','linewidth',2)
hold on
plot(top_p_08,top_y_08,'r','linewidth',2)
hold on
plot(top_p_04,top_y_04,'green','linewidth',2)
title('pressure-deformation curve(y-direction)')
xlabel('pressue,Pa')
ylabel('deformation,m')
legend('the original thickness','0.8 mm thickness','0.4 mm thickness')
set(gca,...
'FontSize',24)

end

```

APPENDIX D

G-code for 3D printing

Start Gcode

```
;TIME:35701                                %estimate time
;Filament used: 5.00416m                    %estimate filament exhaust
;Layer height: 0.06                          %layer height
;Generated with Cura_SteamEngine 3.2.1      %Cura software version
M190 S80                                     %Build plate temperature
M104 S230                                    %extruder temperature
M109 S230                                    %extruder temperature
M82 ;absolute extrusion mode
G21 ;metric values
G90 ;absolute positioning
M82 ;set extruder to absolute mode
M107 ;start with the fan off
G28 X0 Y0 ;move X/Y to min endstops
G28 Z0 ;move Z to min endstops
G1 Z15.0 F9000 ;move the platform down 15mm
G92 E0 ;zero the extruded length
G1 F200 E3 ;extrude 3mm of feed stock
G92 E0 ;zero the extruded length again
G1 F9000
;Put printing message on LCD screen
M117 Printing...
;LAYER_COUNT:280
;LAYER:0
M107
G0 F3600 X89.034 Y132.338 Z0.3
```

;TYPE:SKIRT

End Gcode

;TIME_ELAPSED:35701.498235

G1 F1500 E846.6421

M107

M104 S0 ;extruder heater off

M140 S0 ;heated bed heater off (if you have it)

G91 ;relative positioning

G1 E-1 F300 ;retract the filament a bit before lifting the nozzle, to release some of the pressure

G1 Z+0.5 E-5 X-20 Y-20 F9000 ;move Z up a bit and retract filament even more

G28 X0 Y0 ;move X/Y to min endstops, so the head is out of the way

M84 ;steppers off

G90 ;absolute positioning

M82 ;absolute extrusion mode

M104 S0

;End of Gcode